Programmable self-assembling system to model intracellular protein aggregation and decode neurodegenerative diseases

Yujie Fan[1,2], Jonathan D. Hoang[1,2], Chelsie Steele[1], Yochana Benchetrit[1], Sayan Dutta[1,2], Gerard M. Coughlin[1,2], Nathan Appling[1], Xiaozhe Ding[1], Changfan Lin[1], Zhe Qu[1], Elisha D. Mackey[1], Viviana Gradinaru[1,2,*]

[1] Division of Biology and Biological Engineering, Caltech, Pasadena, CA 91125
[2] Aligning Science Across Parkinson's (ASAP) Collaborative Research Network, Chevy Chase, MD 2081

*Correspondence to: viviana@caltech.edu

Abstract

Pathological protein aggregation is a conserved feature of neurodegenerative diseases. However, slow progression, aggregates heterogeneity and selective vulnerability make it challenging to model diseases and dissect mechanisms. Here, we present a genetically-encoded, modular platform of self-assembling protein that enables inducible, tunable and cell-type-specific formation of intracellular protein aggregates. We engineered self-assembling variants of α-synuclein (SAS), Tau, and TDP-43, recapitulating hallmarks of Parkinson's disease, Alzheimer's disease, and ALS, respectively. SAS formed Lewy body-like inclusions, nucleated endogenous α-synuclein, triggered neuroinflammation and neurite degeneration; Self-assembling-Tau induced tangles formation, extracellular Aβ and severe neurodegeneration; Self-assembling-TDP caused TDP-43 mislocalization and cytoplasmic inclusions with mild degeneration. Notably, the system revealed disease-specific aggregate-organelle interactions. *In vivo*, systemic or dopamine neuron-targeted delivery of SAS induced progressive motor deficits, dopaminergic neuron loss, and microglial activation. Our self-assembling system robustly mirrors histological, transcriptional, and behavioral features of human disease, providing a powerful platform to dissect mechanisms and accelerate therapeutic development.

Keywords

Neurodegenerative diseases; Protein aggregation; Self-assembling protein; Alpha synuclein; Tau; TDP-43; Parkinson's disease; Alzheimer's disease; Amyotrophic lateral sclerosis; Preclinical models.

35 **Graphical abstract**

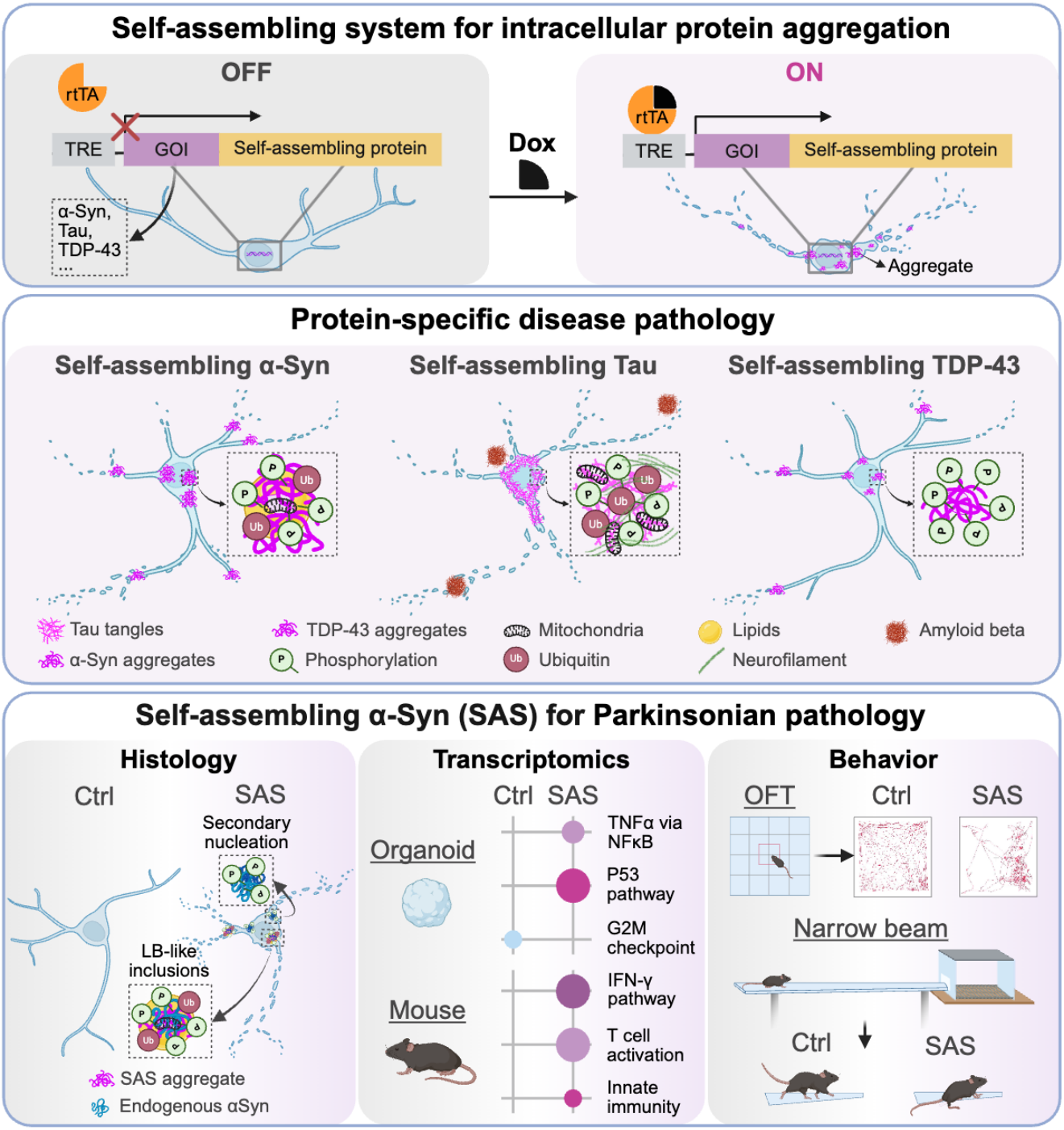

36

Introduction

Protein aggregation is a pathological hallmark of numerous neurodegenerative disorders, including Parkinson's disease (PD), Alzheimer's disease (AD), and amyotrophic lateral sclerosis (ALS)[1]. In these conditions, misfolded proteins form intracellular or extracellular inclusions that disrupt cellular homeostasis, impair organelle function, propagate through neural circuits and eventually lead to neuronal loss and behavioral changes[2,3]. Despite their shared etiology of protein aggregation, different neurodegenerative diseases involve distinct aggregating proteins, affect different brain regions, exhibit unique patterns of cell-type vulnerability, and lead to divergent clinical outcomes[4]. It remains poorly understood which forms of aggregates are toxic, how aggregates spread between cells and drive neurotoxicity, and why certain neurons are more vulnerable to specific protein aggregates than others.

Protein misfolding and aggregation may begin decades before onset of clinical symptoms and the aggregates display substantial heterogeneity across patients[5]. Capturing the slow progression, heterogeneity and cell-type-specific vulnerability characteristic of human proteinopathies in experimental models remains a major challenge. Most existing models rely on toxicants, overexpression of disease-related proteins or exogenous seeding with fibrils. These approaches often lack temporal and cell-type control and fail to recapitulate key aspects of disease pathology. A notable example is PD, which is characterized by the progressive loss of dopaminergic (DA) neurons and the formation of intracellular inclusions known as Lewy bodies (LBs) and Lewy neurites (LNs)[6–8]. The main component of LBs and LNs is misfolded α-synuclein (αSyn). It remains unclear when and where the αSyn aggregation begins, how it spreads between cells, and why the DA neurons are particularly vulnerable to degeneration[9,10]. Numerous *in vitro* and *in vivo* models have been developed to model and study PD[11–13]. Toxicant-based models, such as 6-hydroxydopamine (6-OHDA), induce rapid DA neuron degeneration but typically fail to produce LBs and LNs pathology[14,15]. Genetic models, including overexpression of αSyn, often do not exhibit key pathological hallmarks [16]. More recently, the αSyn pre-formed fibril (PFF) model has gained prominence, as intracerebral injection of αSyn PFFs induces neurodegeneration and behavioral deficits in rodents[17–19]. However, this model requires invasive surgical procedures and lacks cell-type specificity. A system that allows precise and programmable modeling of protein aggregation in defined cell types could transform our ability to study disease mechanisms across diverse neurodegenerative conditions.

Here, we developed a genetically-encoded, modular platform that enables inducible, tunable, and cell-type-specific formation of intracellular protein aggregates across diverse *in vitro* and *in vivo* experimental models. Using this platform, we engineered self-assembling variants of αSyn, Tau, and TDP-43 to model hallmark features of PD, AD, and ALS, respectively. In HEK cells, primary neurons and human brain organoids, self-assembling αSyn (SAS), Tau (SA-Tau) and TDP-43 (SA-TDP) induced histopathology that closely mirrored that in the human diseases, establishing a new paradigm in disease modeling. SAS aggregates formed LB-like inclusions that interacted with

mitochondria, lipids, lysosomes, and ubiquitin, features observed in PD patients but not fully captured by prior experimental models. Applying the same approach to Tau produced hyperphosphorylated tangles that were highly ubiquitinated, elevated neurofilament levels, and promoted extracellular amyloid beta production, resulting in severe neurodegeneration. In contrast, self-assembling TDP-43 formed phosphorylated cytoplasmic inclusions that exhibited minimal interaction with mitochondria and ubiquitin, leading to milder neurodegeneration at comparable expression levels and time. Furthermore, non-invasive, cell-type-specific delivery of SAS to DA neurons in the mouse brain led to motor deficits, DA neuron loss, reduced striatal projections, and propagation of αSyn aggregates from the substantia nigra pars compacta (SNpc) to other brain regions. This system not only recapitulates key histological and transcriptional features of human disease but also enables programmable modeling of aggregate biology across diverse contexts. Our platform provides a powerful, extensible tool to interrogate mechanisms of neurodegeneration and to accelerate therapeutic development.

Results

Self-assembling system induces intracellular protein aggregates and enables tunable proteinopathy

Abnormal protein aggregates in neurodegenerative diseases are composed of not only misfolded protein, but also diverse cellular components[20,21]. Rather than synthesizing pure protein fibrils in solution and then introducing them into cells, we hypothesized that inducing protein aggregation intracellularly would enable the aggregates to incorporate endogenous cellular components, therefore more faithfully recapitulating disease pathology. Previous studies have shown that de novo-designed helical filaments[22,23] and naturally occurring self-assembling proteins[24,25] can form ordered aggregates spontaneously in solution or in yeast. Such self-assembling proteins have been applied to record protein activity *in vivo*[26,27]. Inspired by these studies, we developed a genetically encoded platform for programmable aggregate formation, Focusing initially on αSyn, we designed a library of self-assembling synuclein (SAS) constructs, each consisting of human *SNCA*, the gene encoding αSyn, fused with a different self-assembling protein (SAP) at a position predicted to remain accessible on the exterior surface of the resulting filament (**Table S1**). To enable temporal control, we integrated this design into a doxycycline-regulated system. Cell-type specificity was achieved by utilizing custom promoters to drive expression of the reverse tetracycline-controlled transactivator (rtTA), allowing for targeted induction of αSyn aggregation in desired cell populations (**Fig. 1A**).

In vitro screening in HEK cells identified several constructs that not only formed αSyn aggregates but also induced substantial Ser129 phosphorylation of αSyn (pS129-αSyn), a hallmark of PD pathology (**Fig. 1B and S1A**). Different SASs resulted in different types of aggregates with varying ability to induce pS129-αSyn. Among these, SAS3 formed condensed punctate structures and robustly induced pS129-αSyn. To confirm that the pS129-αSyn induction was specific to the

αSyn aggregates, we compared SAS3 with rtTA-transfected control (Ctrl), *SNCA* overexpression (*SNCA* OE), and SAP alone. Only SAS3 led to strong pS129 induction; Neither αSyn OE nor SAP alone triggered similar pathology (**Fig. 1B**). Western blot analysis revealed that SAS3 induced 1000-fold higher pS129-αSyn compared to *SNCA* OE (**Fig. 1C&D and S1B&C**), underscoring the pathological potency of the construct. To enable real-time visualization of aggregate dynamics, we generated a fluorescent version of SAS3 by replacing the V5 epitope tag with a GFP reporter (SAS-GFP) (**Fig. S1D&E**). Live imaging demonstrated gradual appearance and growth of intracellular αSyn aggregates (**Movie S1**). The SAS system was designed to allow precise control of αSyn aggregation and pathology through manipulation of doxycycline (dox) concentration and treatment duration. Indeed, titration of dox concentration decreased the average number and size of aggregates (**Fig. 1E, F, and G**). Prolonged dox treatment led to a corresponding increase in aggregation and αSyn phosphorylation (**Fig. S1F**).

To assess the generalizability of the self-assembling protein platform beyond synuclein, we next developed analogous constructs targeting two other major neurodegenerative disease proteins: Tau and TDP-43, which are central to AD and ALS, respectively. Using the same modular design as SAS, we fused Tau (2N4R isoform) or TDP-43 to the self-assembling domains used in SAS3 (**Fig. 1H; Table S1**). In HEK cells, self-assembling Tau (SA-Tau) formed fibrillar cytoplasmic tangles that were positive for phospho-Tau (AT8), a hallmark of tauopathy and AD (**Fig. 1I**). Self-assembling TDP-43 (SA-TDP) induced cytoplasmic inclusions and mislocalization of TDP-43 with strong phospho-TDP-43 signal, mirroring ALS pathology (**Fig. 1J**).

Together, these results demonstrate that our self-assembling system enables intracellular formation of protein aggregates, relevant to multiple neurodegenerative diseases. Its compatibility with genetic control, tunability, and modularity provide robust, scalable, and refined preclinical models for studying disease mechanisms and developing therapeutics.

Self-assembling αSyn, Tau, and TDP-43 aggregates recapitulate distinct, protein-specific histopathology in neurons

Another defining feature of neurodegenerative diseases is neuronal degeneration. Having shown that our self-assembling system drives robust, phosphorylated protein aggregation in HEK cells, we next investigated whether these aggregates could trigger neuronal degeneration. We delivered the self-assembling system to mouse primary neurons using adeno-associated virus (AAV) AAV9-X1.1[28], an engineered AAV that efficiently transduces primary murine and human neurons in culture[29] (**Fig. 2A)**. As observed in HEK cells, SAS3 induced prominent αSyn aggregation and pS129-αSyn in both the soma and neurites of primary neurons (**Fig. 2B** and quantified in **Fig. 2C&D**). Notably, SAS3-transduced neurons also exhibited pronounced neurite retraction after 3 days of dox treatment (**Fig. 2B&E**), mimicking the neurodegeneration observed in PD. Consistent with these findings, SAS3 also induced αSyn aggregation and neurite retraction in human embryonic stem cell (hESC)-derived neurons (**Fig. S2A**). Similarly, SA-Tau formed extensive tau

155 tangles positive for phospho-Tau (AT8), accompanied by severe neuronal loss and neurite
156 degeneration as marked by MAP2 (**Fig. 2F**). Intriguingly, SA-Tau expression also led to elevated
157 levels of extracellular amyloid beta (Aβ) (**Fig. 2G**), suggesting a potential link between
158 intracellular Tau aggregation and Aβ dysregulation. Neurons expressing SA-TDP exhibited
159 cytoplasmic TDP-43 inclusions with strong pTDP-43. However, compared with equivalent
160 expression of SAS and SA-Tau, SA-TDP induced milder neurodegeneration (**Fig. 2H**). Total TDP-
161 43 staining revealed translocation of endogenous TDP-43 from the nucleus to cytoplasm and
162 aggregation (**Fig. 2I**). Collectively, these findings establish that the self-assembling protein
163 aggregates not only induce neurodegeneration, but also recapitulate distinct, protein-specific
164 pathological signatures.

165 **Self-assembling system reveals distinct organelle interactions and pathological signatures of**
166 **αSyn, Tau, and TDP-43 aggregates in human brain organoids**

167 How different protein aggregates drive distinct neurotoxicity remains poorly understood. We
168 hypothesized that differential interactions between protein aggregates and other cellular
169 components may underlie their varying toxic effects, contributing to the pathogenesis of different
170 neurodegenerative diseases[30]. Supporting this idea, postmortem examination of PD patients has
171 shown that aggregates are far from homogeneous lumps of toxic protein[31]. LBs often contain
172 hundreds of different proteins and even entire membranous organelles tangled up in them[32,33]. One
173 considerable advantage of the self-assembling system is its ability to drive intracellular
174 aggregation, potentially enabling incorporation of other cellular components and better
175 recapitulation of the molecular complexity of pathological inclusions.
176
177 To test this hypothesis in a physiologically relevant context, we delivered SAS, SA-Tau and SA-
178 TDP43 to hESC-derived brain organoids using AAV-X1.1 (**Fig. 3A**). Organoids produce diverse
179 cell types in a 3D environment that closely mimics the function and structure of *in vivo*
180 counterparts. While organoids have been widely used for modeling neurodevelopment, existing
181 organoid models often fail to display hallmark features of neurodegenerative diseases, such as LB
182 formation and neuronal degeneration in PD[34]. In particular, αSyn PFFs, which have shown promise
183 in animal studies, are inefficient in organoids due to limited uptake and poor tissue penetration
184 (**Fig. 3B**). In contrast, AAV-delivered SAS3 was able to efficiently access the entire organoids.
185 Immunostaining for the V5 tag and pS129-αSyn revealed widespread synucleinopathy, with
186 aggregates present even in deep layers of organoids (**Fig. 3B and S3A&B**). Similarly, SA-Tau and
187 SA-TDP produced hallmark pathologies of AD and ALS in human brain organoids, including
188 phosphorated Tau tangles and TDP-43 aggregates, extracellular Aβ accumulation, and cytoplasmic
189 TDP-43 inclusions (**Fig. S3D-G**). Together, these findings establish the self-assembling system as
190 a robust platform for modeling and investigating authentic inclusion biology in a human-relevant
191 system, filling a major gap in current disease models.
192

To investigate the molecular composition and cellular impact of aggregates, we performed confocal Z-stack imaging of organoids infected with self-assembling constructs and stained for cellular components. In SAS-expressing organoids, co-staining for the V5 tag to trace aggregates and the mitochondrial membrane marker TOMM20 revealed clear TOMM20 signal within the αSyn aggregates, indicating that mitochondria were sequestered in the inclusions (**Fig. 3C**), a feature not observed in control groups (**Fig. S3C**). SAS-induced inclusions were highly ubiquitinated (**Fig. 3D**) and showed prominent accumulation of autophagy adaptor p62/SQSTM1 in and around the aggregates (**Fig. 3E**), suggesting these inclusions are recognized and targeted by protein clearance pathways. Nile red staining revealed that aggregates were enriched in lipids (**Fig. 3F**), a common feature of LBs from PD patient brains. Tau and TDP-43 aggregates displayed distinct aggregate-organelle interaction profiles. In SA-Tau-expressing organoids, mitochondria accumulated around the aggregates rather than being trapped inside (**Fig. 3G**). Tau tangles were also highly ubiquitinated (**Fig. 3H**), p62-positive (**Fig. S3F**) and colocalized with neurofilament light chain (NfL) **(Fig. 3I)**. In contrast, SA-TDP-induced aggregates showed minimal co-localization with mitochondria, ubiquitin, or NfL, but still induced p62 accumulation (**Fig. 3J and S3H-J**). This divergence in aggregate-organelle interactions (**Fig. 3K**) may explain the milder neurodegeneration observed in SA-TDP-expressing organoids and primary neurons compared to SAS and SA-Tau.

Self-assembling protein system recreated protein-specific aggregation and disease-relevant pathology in human brain organoids and uncovered distinct aggregate-organelle interaction profiles that might underlie differential aggregates toxicity. The ability to resolve these aggregate-specific signatures provides a unique opportunity to dissect the molecular basis of selective vulnerability in PD, AD, ALS, and other related disorders.

SAS forms LB-like inclusions and nucleate aggregation of endogenous αSyn, triggering neuronal inflammation and death.

Having established our self-assembling system faithfully recapitulates protein-specific pathology across neurodegenerative diseases, we next focused on PD to further explore the full potential of SAS in elucidating mechanisms of αSyn-mediated neurodegeneration. Our findings demonstrated that SAS induced complex, multi-component inclusions that closely resemble human LBs in terms of molecular composition[38] (**Fig. 3C-F**). Here, we further showed the inclusion also recapitulate key morphological features of LBs. Thioflavin S staining confirmed the presence of β-sheet–rich fibrillar content in SAS-expressing neurons (**Fig. S4A**). Notably, the Thioflavin S signal often extended beyond the V5-positive core, suggesting the existence of secondary aggregated species. Co-staining of the V5 tag and pS129-αSyn revealed numerous V5-negative and pS129-αSyn-positive aggregates, pointing to the formation of endogenous αSyn inclusions (**Fig. S4B**). PD is widely considered a prion-like disease, in which abnormal αSyn aggregates can induce secondary nucleation of normal αSyn[35–37], promoting disease spreading. To determine whether SAS-induced aggregates possess this capability, we used primary neurons carrying an SNCA-GFP reporter,

233 enabling tracking of the endogenous αSyn (**Fig. 4A**). Following 36 hours of dox treatment, neurons
234 expressing SAS3 exhibited degeneration phenotypes compared with control groups (**Fig. 4B**), with
235 further worsening by 72 hours (**Fig. S4C**). Close examination of SAS3-transduced neurons
236 revealed endogenous αSyn aggregation in both soma and neurites (**Fig. 4C**), confirming a prion-
237 like seeding effect.
238
239 To better understand the mechanisms of SAS-induced neurodegeneration, we conducted bulk
240 RNAseq of SAS-transduced and control organoids. SAS-expressing organoids displayed a distinct
241 transcriptomic profile (**Fig. 4D**), with 178 differentially expressed genes (DEGs) with adjusted p-
242 value < 0.05 and $|\log_2$ fold change (FC)| >1 (**Fig. S4D** and **Table S2**). Pathway analysis revealed
243 significant upregulation of p53 and TNFα signaling, key regulators of apoptosis and inflammation
244 (**Fig. 4E**). Notably, the TNF-NF-κB-p53 axis has been demonstrated to mediate dopamine neuron
245 survival in neuron transplant experiments[39]. Targeting this pathway might enhance neuron survival
246 in PD. Consistent with human transcriptomic data[40], SAS-treated organoids showed activation of
247 apoptosis, inflammation, and mitochondrial dysfunction pathways (**Fig. 4F and S4E**). In line with
248 transcriptomic findings, immunostaining for the astrocyte marker GFAP revealed astrocyte
249 activation surrounding SAS-expression neurons and active engagement with protein inclusions
250 (**Fig. 4G**). Among the top 50 most dysregulated genes, many were previously implicated in PD
251 (**Fig. 4H**). For example, *FDXR*, which encodes the mitochondrial ferredoxin reductase that helps
252 produce iron-sulfur clusters, has been linked to inflammation-associated neurodegeneration[41],
253 consistent with our earlier finding that SAS inclusions sequester mitochondria (**Fig. 3C**).

254 These results illustrated that SAS induced both primary and secondary αSyn aggregation, forming
255 inclusions that resemble human LBs in molecular composition, morphology and pathogenic
256 function. Further, these inclusions triggered TNFα-mediated neuroinflammation, glial activation
257 and ultimately neuronal death.
258
259 **Brain-wide delivery of SAS induces PD-relevant histopathology and behavioral deficits in**
260 **mice**

261 The primary clinical manifestation of PD is movement disorder. To investigate whether SAS can
262 induce behavior abnormalities *in vivo*, we utilized AAV-PHP.eB, an AAV capable of crossing the
263 blood-brain barrier (BBB) after systemic injection, to achieve non-invasive delivery of SAS into
264 the mouse central nervous system (CNS)[42]. To specifically target neurons, we used the human
265 synapsin (hSyn) promoter to drive the expression of rtTA. The hSyn-rtTA and TRE-SAS3
266 constructs were packaged into AAV-PHP.eB and co-delivered into wild-type (WT) C57BL/6J
267 mice via retro-orbital (RO) injection. Dox treatment started 2 weeks after virus injection and open
268 field test (OFT) assay were performed every other week (**Fig. 5A**). After 4 weeks of dox treatment,
269 SAS3-treated mice exhibited a progressive decline in movement in the OFT compared to control
270 groups (**Fig. 5B**). After 8 weeks, mice were sacrificed for histological analysis to assess
271 neuropathological changes associated with SAS3 treatment. We first examined the substantia nigra

272 (SN) and observed aggregates in both SN pars compacta (SNpc) and reticulata (SNr). Strikingly,
273 the SNpc exhibited a clear reduction in TH+ neurons (**Fig. 5C**), and the intensity of DA neuron
274 projections was significantly diminished in the striatum (**Fig. 5D&E**). Next, we examined the
275 olfactory bulb (OB), which PHP.eB strongly transduces. Consistent with our *in vitro* findings,
276 SAS-induced aggregates were associated with robust pS129-αSyn staining, whereas the control
277 (hSyn-rtTA only), *SNCA* OE, and SAP treatments did not induce significant pS129-αSyn signal
278 (**Fig. 5F and S5A**). Aggregates were also found in other brain regions such as cortex and
279 hippocampus (**Fig. S5B** and see **Movie S2** for aggregate distribution in a cleared whole brain).
280 Finally, proteinase K treatment of a SAS3-transduced brain confirmed the resistance of the
281 aggregates to proteolytic degradation (**Fig. 5G**), further supporting their pathological relevance.

282 **Dopaminergic neuron-targeted SAS recapitulates progressive motor dysfunction and αSyn**
283 **aggregate propagation in mice**

284 As a genetically encoded system, SAS provides a well-defined platform to dissect the roles of
285 specific cell types in PD pathology. Degeneration of DA neurons in the SNpc causes motor
286 symptoms in PD[43]. To selectively deliver SAS3 into DA neurons, we injected Cre-dependent SAS3
287 (DIO-SAS3) into TH-Cre mice using AAV-PHP.eB (**Fig. 5H**). 4 weeks post virus injection, SAS3-
288 treated mice started to exhibit significant motor impairments in the beam-crossing assay, requiring
289 more time to traverse the beam (**Fig. S6A**) and displaying an increased number of slips (**Fig. 5I**)
290 compared to control mice. The motor deficits progressively worsened with prolonged dox
291 treatment, indicating ongoing neurodegeneration. Mice were sacrificed at 4, 8 and 12 weeks for
292 histological analysis to assess the progression of pathology. We first examined DA neurons in the
293 SN (**Fig. 5J and S6B**). At week 4, SAS-induced aggregates were primarily detected in DA neurons
294 within the ventral tegmental area (VTA) and SNpc. By week 8, the number of aggregates had
295 increased, and many TH+ neurons in the SNpc exhibited a clear reduction in TH expression (**Fig.**
296 **S6B**). At week 12, while most neurons with aggregates in the VTA retained TH expression, a
297 significant proportion of neurons in the SNpc with aggregates exhibited markedly reduced or
298 absent TH expression (**Fig. 5J**). We also detected SAS-induced aggregates in regions that are not
299 typically targeted by TH-Cre, suggesting potential propagation of aggregates beyond DA neurons.
300 A similar trend was observed in the striatum, the primary target of DA neurons from the SNpc. At
301 week 4, no aggregates were detectable in the striatum (**Figure S6C**). However, aggregates
302 emerged by week 8 (**Fig. S6C**) and became more prominent by week 12 (**Fig. 5K**), suggesting
303 progressive aggregate accumulation and potential spreading along the nigrostriatal pathway. The
304 intensity of TH staining in the striatum also decreased with time (**Fig. 5K and S6C**), reflecting a
305 reduction in dopaminergic innervation, consistent with the observed neurodegeneration in the
306 SNpc. Immunostaining for V5 and pS129-αSyn revealed that not only were SAS-induced
307 aggregates strongly phosphorylated (**Fig. S6D, arrows**), but a significant amount of endogenous
308 α-synuclein also aggregated and became phosphorylated (**Fig. S6D, arrowheads**). This again
309 confirmed that SAS3 can induce secondary nucleation of αSyn, contributing to the spread of

disease. Ubiquitin and p62/SQSTM1 immunostaining confirmed the molecular complexity of the SAS-induced aggregates and their resemblance to LBs **(Fig. 5L&M)**.

Targeting SAS expression to DA neurons recapitulated multiple hallmarks of Parkinson's disease, from motor impairment and dopaminergic degeneration to αSyn propagation and LB-like inclusion formation. These results establish SAS as a mechanistically informative platform for probing selective vulnerability and intercellular aggregate dynamics *in vivo.*

SAS activates microglia and triggers immune response in mice

To dissect transcriptional changes in response to SAS-induced aggregates *in vivo*, we performed bulk RNAseq of the OB, a region strongly transduced by PHP.eB and one of the earliest and consistently affected brain regions in PD. SAS-transduced mice displayed a distinct transcriptome compared with control mice expressing only rtTA (**Fig. 6A**). Differential gene expression analysis identified 139 DEGs with adjusted p-values < 0.05 and $|\log_2 FC| > 1$ (**Table S3**), with a strong enrichment of genes promoting inflammation (**Fig. 6B**). Pathway analysis confirmed robust activation of inflammatory and immune responses (**Fig. 6C and S7A**). Among the top 50 most dysregulated genes (**Fig. 6D**), several key inflammatory pathways were highly upregulated, including interferon-gamma (IFN-γ), tumor necrosis factor-alpha (TNF-α), toll-like receptor (TLR), and interleukin (IL) signaling (**Fig. 6E**).

We also observed a significant upregulation of genes associated with microglial activation in SAS-transduced mice (**Fig. 6F**). For example, IBA1, encoded by the *Aif1* gene, was markedly increased in SAS3-treated mice. CXCL9, a chemokine produced by microglia that plays a crucial role in neuroimmune responses, exhibited an approximately 500-fold upregulation. CST7, a cystatin that has been implicated in microglial activation under disease conditions and is linked to pathways involved in phagocytosis, cytokine/chemokine signaling, and antigen presentation, was also highly expressed. Additionally, complement protein C3, a key activator of microglia, showed a 60-fold increase. These changes strongly indicate a pronounced microglial activation state in SAS3-treated mice. Immunostaining of astrocytes (GFAP) and microglia (IBA1) confirmed that activated microglia clustered around SAS-induced aggregates, suggesting a targeted immune response to pathological protein accumulation (**Fig. 6G and S7B**). Collectively, these findings highlight the profound neuroinflammatory impact of SAS-induced aggregates, mirroring key aspects of PD pathology.

Discussion

In this study, we present a synthetic biology platform that enables inducible, tunable, and cell-type-specific formation of intracellular aggregates of disease-relevant proteins in diverse model systems. This platform faithfully recreates hallmark features of human proteinopathies *in vitro* and *in vivo*, including inclusion localization, morphology and composition, transcriptional responses, and behavioral phenotypes. Using self-assembling α-synuclein (SAS), we established a PD model

348 that recapitulates Lewy body-like pathology, dopaminergic neuron loss, aggregate propagation
349 along the nigrostriatal axis, and progressive motor deficits. Importantly, SAS-induced aggregates
350 incorporate mitochondria, lipids, ubiquitin, and p62, molecular signatures of bona fide Lewy
351 bodies that have been difficult to reproduce in other disease models. The system also revealed
352 prion-like seeding of endogenous αSyn and elicited robust glial responses, offering a powerful
353 framework to study cell-nonautonomous aspects of disease progression. Moreover, by extending
354 this approach to Tau and TDP-43, we demonstrated the platform's generalizability across major
355 neurodegenerative diseases. The observed differences in organelle interactions and toxicity of
356 different protein aggregates illuminate potential mechanisms of selective vulnerability and disease
357 divergence.
358
359 During our initial SAS construct screening, we discovered that different types of αSyn aggregates
360 exhibit widely varying capacities to induce pS129-αSyn, a key disease marker. This raises critical
361 questions about what structural and biochemical features define a toxic aggregate. Our findings
362 suggest that local concentration, structural conformation, and context-dependent modifications
363 play a decisive role. For example, SAS3-induced aggregates exhibit significantly higher toxicity
364 than *SNCA* OE despite a lower total amount of αSyn (**Fig. 1C-D and S1B-C**). Similar observations
365 have been made comparing αSyn PFFs and αSyn monomers. Structural differences appear to
366 influence pathological outcomes, as different SAS constructs induce different levels of toxicity
367 and phosphorylation (**Fig. S1A**). This aligns with studies showing that patient-derived αSyn PFFs
368 exhibit different structural properties and varying neurotoxicity[44]. These observations imply that
369 the structural conformation of αSyn aggregates may be a key determinant of disease progression
370 and severity. Deciphering the structural determinants of aggregate toxicity may be essential for
371 understanding disease progression and designing targeted interventions.
372
373 A major strength of this platform is its broad applicability across *in vitro* and *in vivo* experimental
374 systems, including cell lines (**Fig. 1**), primary neurons (**Fig. 2**), hESC or iPSC-derived neurons,
375 organoids (**Fig. 3&4**), and mice (**Fig. 5-6**). Notably, in hESC-derived neurons and brain organoids,
376 SAS, SA-Tau and SA-TDP enable robust recapitulation of PD, AD, and ALS hallmarks, such as
377 LB formation, extracellular Aβ production, and TDP-43 cytoplasmic inclusions, which previous
378 models have failed to reproduce. This provides a compelling opportunity to integrate our self-
379 assembling system with patient-derived iPSCs to dissect the impact of genetic variants and
380 environmental factors on disease onset and progression. The system's tunability also makes it well
381 suited for high-throughput screens to identify disease modifiers and therapeutic compounds.
382
383 We provide direct evidence in primary neurons that SAS induces secondary nucleation of
384 endogenous αSyn (**Fig. 4B&C**). This finding is further supported by the presence of V5-negative,
385 pS129-positive aggregates in neurons in multiple, *in vitro* and *in vivo*, systems (**Fig. 2B; Fig. S2A;**
386 **Fig. S3A; Fig. S4B; Fig. S6D**). Secondary nucleation is a critical driver of αSyn aggregation
387 spread and amplification, yet its underlying mechanism remains unclear. Future studies are needed

388 to dissect how primary nucleation triggers secondary nucleation and, more importantly, to identify
389 strategies to halt secondary nucleation, which could be key to developing effective disease-
390 modifying therapies for PD.
391
392 Neurodegenerative diseases often exhibit selective neuronal vulnerability[10], and single-cell RNA
393 sequencing (scRNA-seq) studies have identified distinct neuronal subtypes that are more
394 susceptible to degeneration in PD[45,46]. In this study, we successfully demonstrated the ability to
395 deliver SAS into specific neuron types non-invasively using AAV-PHP.eB. By targeting different
396 neuronal subpopulations using cell-type-specific Cre lines or promoters, we can systematically
397 investigate the roles of various neuronal populations in driving diverse neurodegenerative
398 pathologies. This approach provides a powerful strategy to dissect the contributions of specific
399 neuronal populations to disease progression, offering insights into why certain neurons are
400 particularly susceptible and identifying potential therapeutic targets to protect these vulnerable
401 populations.
402
403 While our primary focus was PD, αSyn aggregation is also central to other synucleinopathies, such
404 as dementia with Lewy bodies (DLB) and multiple system atrophy (MSA)[9]. The SAS system can
405 be readily extended to study these disorders, investigating potentially distinct or overlapping
406 pathological mechanisms. More broadly, our synthetic approach provides a modular,
407 programmable framework for modeling protein aggregation across a wide range of diseases. By
408 applying this strategy to αSyn, Tau and TDP-43, we successfully recapitulated key features of PD,
409 AD and ALS, respectively. By enabling side-by-side comparison of different disease-associated
410 aggregates in a unified system, this platform opens the door to comparative pathology studies and
411 mechanistic discovery across the neurodegenerative disease spectrum. In addition, protein
412 aggregation is increasingly recognized in non-neurological diseases. For example, islet amyloid
413 polypeptide (IAPP) aggregation cause β-cell dysfunction in type 2 diabetes, and aggregation of
414 mutant p53 has been implicated in solid tumors. As such, this platform may hold value for a broad
415 range of research communities beyond neuroscience.
416
417 Together, our work introduces a scalable, versatile and highly disease-relevant strategy to model
418 and dissect protein aggregation. This "build-to-understand" framework sets the stage for
419 fundamental discoveries into the mechanisms of aggregation-driven pathology and for the
420 development of effective, disease-modifying therapies.

421 **Limitations of the study**

422 While the self-assembling protein platform provides a powerful and programmable system to
423 model intracellular protein aggregation and its pathological consequences, it has several
424 limitations. First, although the aggregates recapitulate key disease hallmarks, the precise
425 biophysical structures of the self-assembling aggregates may differ from endogenous protein
426 aggregates found in patients. However, the heterogeneity of intracellularly forming aggregates,

427 both in human patients and our system, present a technical challenge for high resolution structural
428 characterization. In future studies, when technology and resources permit, in situ structural
429 analysis of aggregates may offer more deeper insight into the relationship between aggregate
430 structure and neurotoxicity. Second, our current study is intended as a conceptual and technical
431 advance in the modeling of protein aggregation diseases. Due to the time and resource constrains,
432 we selected SAS3 variant to conduct further studies based on its robust ability to recapitulate
433 Parkinson's disease pathology. However, this doesn't preclude the possibility of other constructs,
434 if tested at a longer duration or in different context, might yield aggregates that more closely
435 resemble disease pathology. Finally, although we demonstrate *in vitro* applicability in human brain
436 organoids and *in vivo* in the mouse, future studies are needed to assess the aggregates in more
437 complex or long-lived models, such as non-human primates. Despite these limitations, our
438 platform offers unprecedented spatiotemporal control and disease relevance, and we envision its
439 broad utility in mechanistic investigations and therapeutic development.

440 Resource availability

441 Lead contact

442 Further information and requests for resources and reagents should be directed to, and will be
443 fulfilled by, the lead contact, Dr. Viviana Gradinaru (viviana@caltech.edu).
444

445 Materials, data and code availability

446 The data, code, protocols, and key lab materials used and generated in this study are listed in a
447 Key Resource Table alongside their persistent identifiers at Table S4. The bulk transcriptomics
448 data generated and analyzed in this study have been deposited in the NCBI Sequence Read Archive
449 (SRA) under BioProject accession number PRJNA1227536. The raw sequencing data and
450 associated metadata are publicly available and can be accessed via the NCBI SRA database at
451 https://www.ncbi.nlm.nih.gov/bioproject/PRJNA1227536. All code associated with analysis and
452 plotting are available from https://github.com/jdthoang/FanY_2025_SAS.

453 Acknowledgments

454 We thank Dr. Catherine Oikonomou for comprehensive editing of the manuscript, and Dr. Sarkis
455 Mazmanian and Dr. Michael Elowitz for helpful discussions. We thank Patricia Anguiano for
456 logistical assistance, and Karan Mahe and the rest of Gradinaru laboratory for critical feedback on
457 the research and manuscript. This work was supported by the Office of Laboratory Animal
458 Resources, CLOVER Center, and Millard and Muriel Jacobs Genetics and Genomics Laboratory
459 at the California Institute of Technology. Figures contain images created with BioRender.com.
460 Y.F. is supported by Caltech Chen Postdoc Innovator Grant and Parkinson's Foundation
461 Postdoctoral Fellowship award PF-PRF-1435603. This research was funded in part by Aligning
462 Science Across Parkinson's (ASAP-020495 to V.G.) through the Michael J. Fox Foundation for

Parkinson's Research (MJFF). For the purpose of open access, the authors have applied a CC BY public copyright license to all Author Accepted Manuscripts arising from this submission.

Author contributions

Y.F. conceived the project, wrote the manuscript and prepared figures with input from all authors. V.G., G.M.C., C.S., J.D.H. assisted in manuscript preparation. Y.F. performed most experiments and collected and analyzed the data. J.D.H. performed the analysis of all RNA-seq data and contributed to animal experiments. C.S. performed all behavior assays, contributed to primary neuron, RNAseq and histology experiments, and assisted in many experiments. Y.B. contributed to cloning, RNAseq and organoid experiments. S.D. contributed to primary neuron and histology experiments. G.M.C. contributed to animal experiments. N.A. contributed to cloning and virus production. X.D. contributed to design of constructs. C.L. contributed to western blotting. Z.Q. contributed to virus production. E.D.M. contributed to primary neuron experiments. V.G. supervised all aspects of this study and funded the project.

Declaration of interests

V.G. is a co-founder and member of the board of directors of Capsida Therapeutics, a fully integrated AAV engineering and gene therapy company. Y.F. and V.G. are inventors of a provisional patent (CIT-9283-P) filed by Caltech on the system described in this study. The remaining authors declare no competing interests.

Fig 1: Self-assembling system induces intracellular protein aggregates and enables tunable proteinopathy.

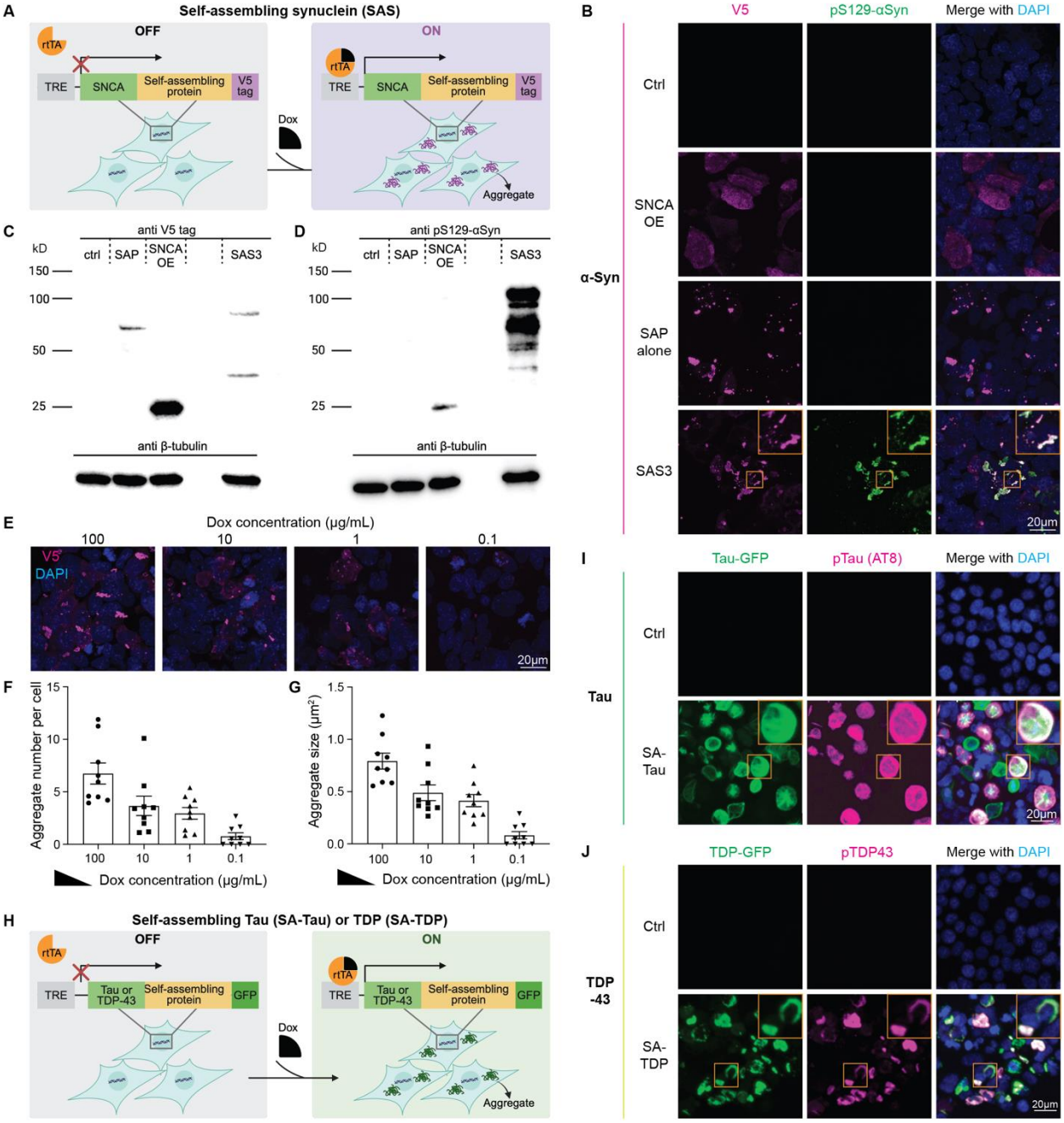

482

483 **Fig. 1. Self-assembling system induces intracellular protein aggregates and enables tunable**
484 **proteinopathy.**
485
486 **(A)** Design of self-assembling synuclein (SAS) system. SAS consists of αSyn fused with a self-assembling
487 protein. In HEK cells, rtTA expression is driven by the EF1α promoter. Upon doxycycline (dox) induction,
488 SAS forms αSyn aggregates intracellularly. **(B)** Screening of SAS constructs in HEK cells. Compared to
489 ctrl (rtTA-transfected only), *SNCA* overexpression (*SNCA* OE) or self-assembling protein (SAP) alone,
490 SAS3 induces αSyn aggregation and strong αSyn S129 phosphorylation after 3 days of dox treatment in
491 transfected HEK cells. **(C-D)** Western blot analysis of total expression (V5 tag, **C**) and pS129-αSyn (**D**),
492 reveals SAS3-induced aggregates trigger markedly stronger αSyn phosphorylation than *SNCA* OE,
493 suggesting enhanced pathogenic potential. n=3 biological replicates. **e,** Representative images of SAS-
494 induced aggregates at varing dox concentration. **(F-G)** Quantification of aggregate number per cell (**F**) and
495 average aggregate size (**G**) for different dox concentrations, demonstrating tunability of the system. n=9
496 biological replicates. **(H)** Schematic of modular design for self-assembling Tau (SA-Tau) and self-
497 assembling TDP-43 (SA-TDP), in which human Tau (isoform 2N4R) or TDP-43 is fused with the same
498 self-assembling protein used in SAS3. A GFP tag is used to detect aggregates. **(I)** Immunostaining of HEK
499 cells transduced with SA-Tau-GFP and stained for pTau (AT8) after 3 days of dox induction shows robust
500 Tau aggregation and hyper phosphorylation. **(J)** Immunostaining of SA-TDP-GFP-expressing HEK cells
501 after 3 days of dox induction reveals cytoplasmic TDP-43 inclusions with strong pTDP-43 signal. Scale
502 bars equal 20 μm. Data are presented as mean ± SEM.

Fig S1: Screening of SAS constructs in HEK cells and tunability of the SAS system.

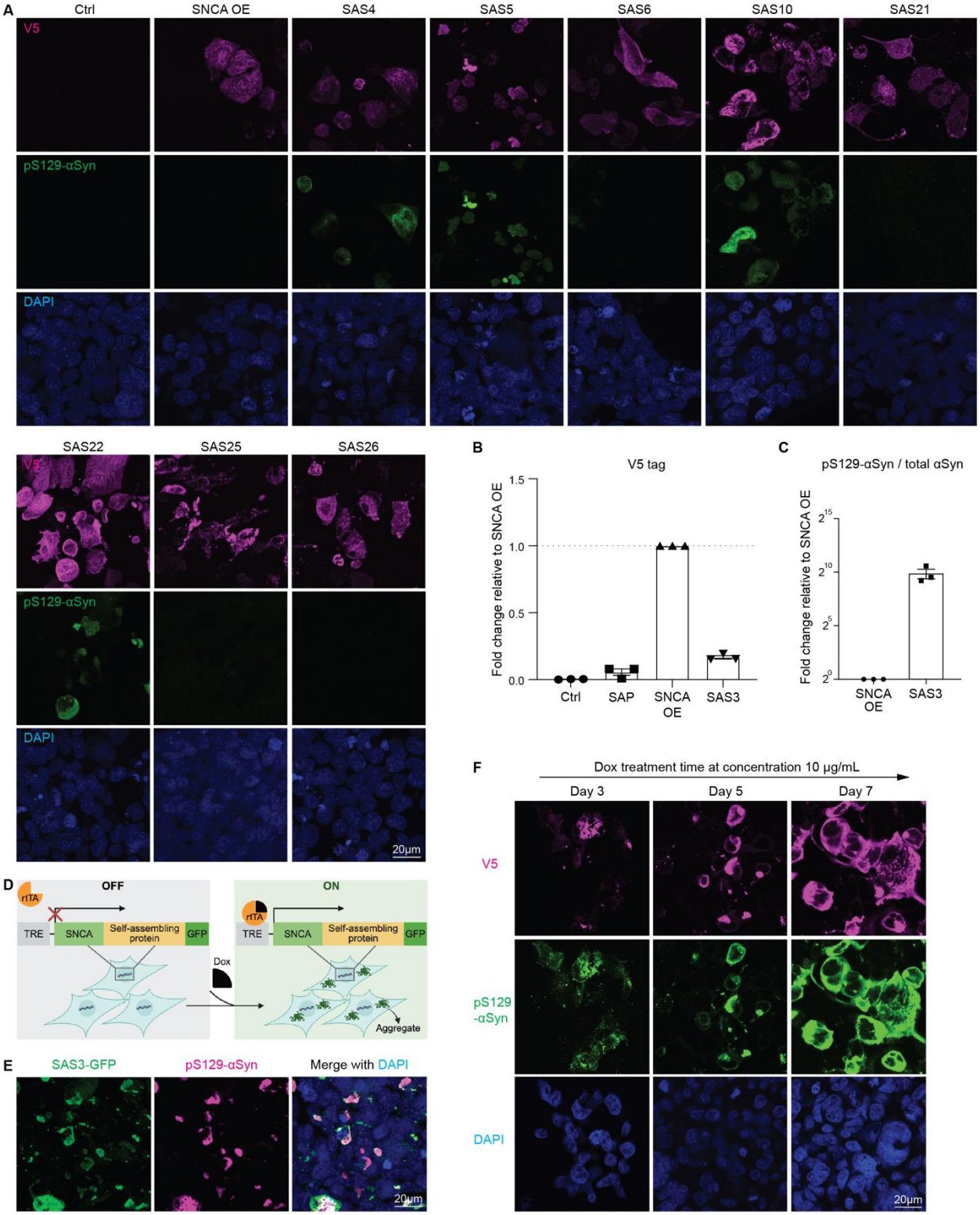

503

504 **Fig. S1. Screening of SAS constructs in HEK cells and tunability of the SAS system.**

505 **(A)** Screening in HEK cells to identify SAS constructs that form αSyn aggregates and induce substantial
506 Ser129 phosphorylation of αSyn. **(B-C)** Quantification of western blot for total expression (V5 tag) and
507 pS129-αSyn show that although SAS3 expression is lower than *SNCA* overexpression (*SNCA* OE), it
508 induces 1000-fold greater phosphorylation, indicating that the enhanced pS129-αSyn signal is due to
509 aggregation rather than protein level. n=3 biological replicates. **(D)** Design of SAS construct with GFP
510 reporter. **(E)** Immunostaining of pS129-αSyn with GFP reporter after 3 days of dox induction,
511 demonstrating that the GFP tag does not alter SAS behavior. **(F)** Immunostaining of V5 tag and pS129-
512 αSyn after 3, 5, and 7 days of dox-induced SAS3 expression, demonstrating that aggregate size and level
513 of pS129-aSyn increase with induction time. Scale bars equal 20 μm. Data are presented as mean ± SEM.

Fig 2: Self-assembling αSyn, Tau, and TDP-43 aggregates recapitulate distinct, protein-specific histopathology in neurons.

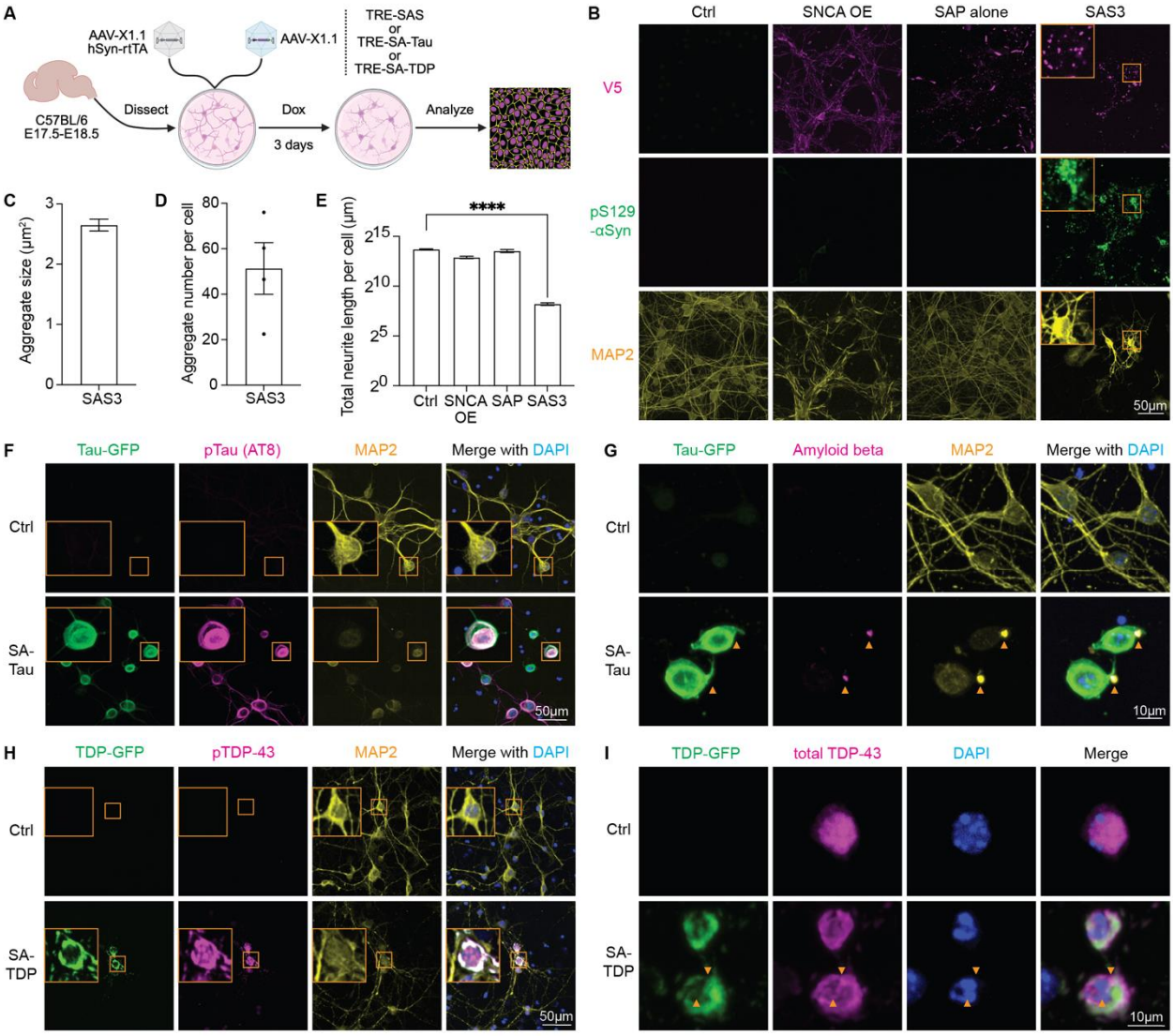

514

515 **Fig. 2. Self-assembling αSyn, Tau, and TDP-43 aggregates recapitulate distinct, protein-specific**
516 **histopathology in neurons.**

517 **(A)** Experimental design for testing the self-assembling system in mouse primary neurons, which is
518 delivered by AAV9-X1.1. In primary neurons, rtTA expression is driven by the hSyn promoter. **(B)**
519 Immunostaining of V5 tag, pS129-αSyn, and MAP2 in transduced primary neurons after 3 days of dox
520 treatment, showing robust αSyn aggregation and pS129-αSyn in both the soma and neurites of neurons, as
521 well as neurite retraction. **(C)** Quantification of average aggregate size induced by SAS3 in mouse primary
522 neurons. **(D)** Average number of aggregates per cell. **(E)** Quantification of total neurite length per cell. n=4
523 biological replicates. ****$p<0.0001$. **(F)** Immunostaining of GFP, pTau (AT8 antibody), and MAP2 in SA-
524 Tau-transduced neurons after 3 days of dox treatment, reveals robust Tau aggregation, hyper pTau, and
525 pronounced neurite degeneration. Enlarged images demonstrate that SA-Tau and SASs form distinct
526 aggregate structures, despite the use of the same self-assembling protein. **(G)** Immunostaining for amyloid
527 beta in primary neurons expressing SA-Tau indicates Tau tangles promote the production of extracellular
528 amyloid beta (arrowhead). **(H)** Representative images of neurons expressing SA-TDP after 3 days of dox
529 treatment show cytoplasmic TDP-43 inclusions with strong pTDP-43. Compared with equivalent
530 expression of SAS and SA-Tau, SA-TDP induces milder neurodegeneration. **(I)** Immunostaining for total
531 TDP-43 reveals translocation of endogenous TDP-43 from nucleus to cytoplasm and aggregation
532 (arrowhead). Scale bar equals 50 μm in **B**, **F, H,** and 10 μm in **G, I**. Data are presented as mean ± SEM;
533 statistical analysis was performed using ANOVA with Dunnett's test.

534
535

Fig S2: SAS induces αSyn aggregation and neurite retraction in hESC-derived neurons.

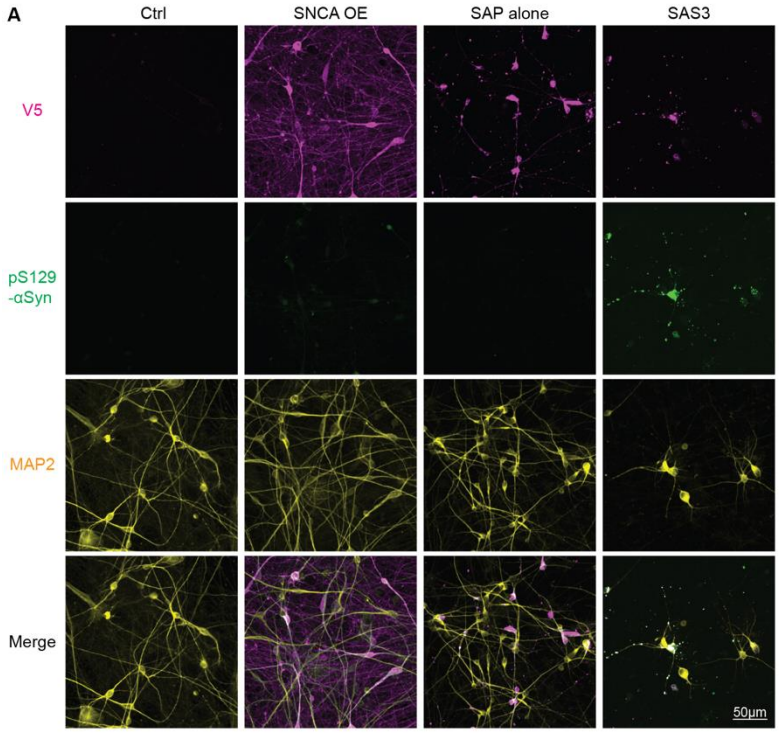

536

537 **Fig. S2. SAS induces αSyn aggregation and neurite retraction in hESC-derived neurons.**

538 **(A)** Immunostaining of V5 tag and pS129-αSyn in transduced hESC-derived human cortical neurons after
539 3 days of dox treatment shows that SAS3 induces αSyn aggregation, strong αSyn phosphorylation, and
540 neurite retraction. Scale bar equals 50 μm.

Fig 3: Self-assembling system reveals distinct organelle interactions and pathological signatures of αSyn, Tau, and TDP-43 aggregates in human brain organoids.

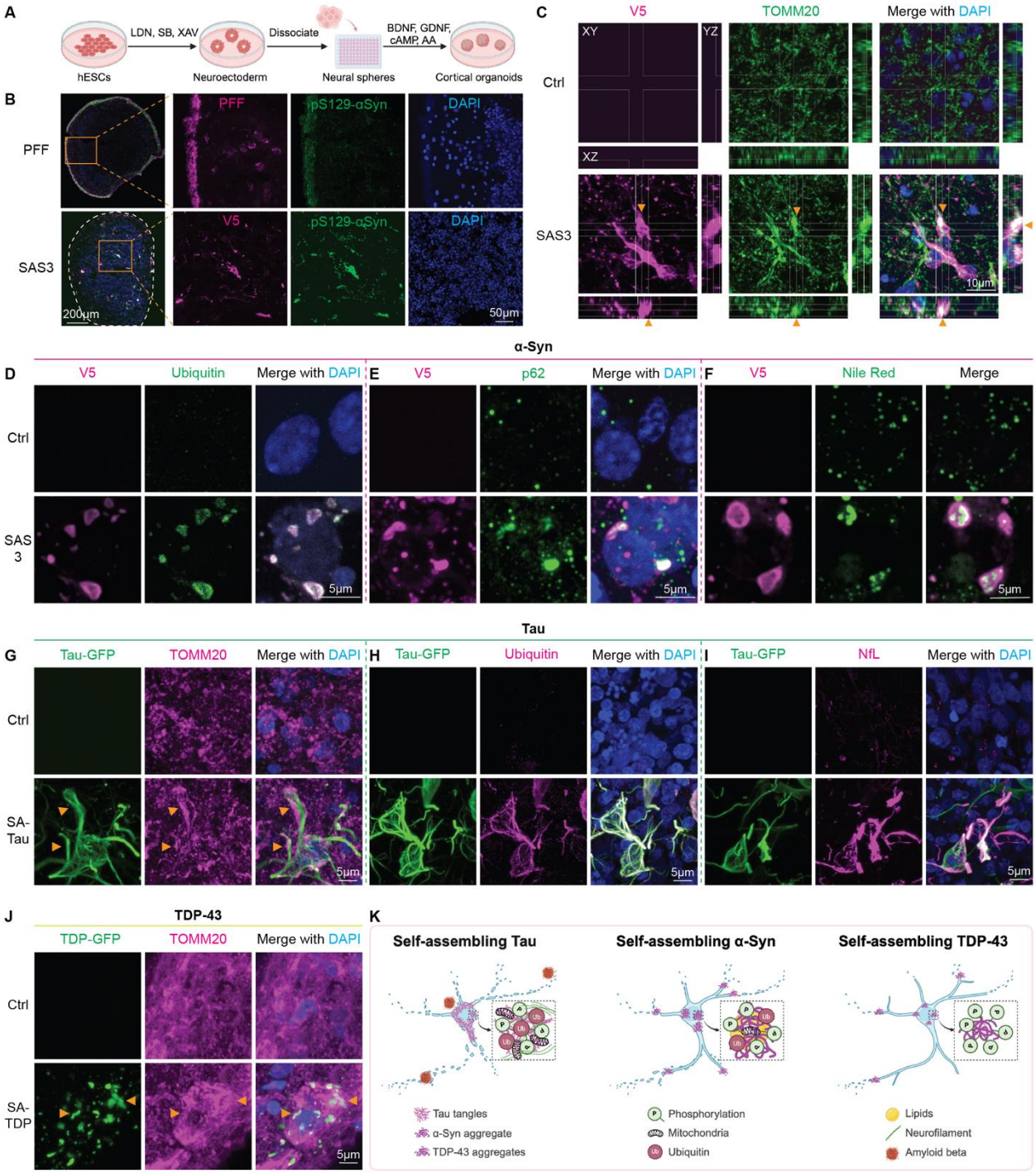

541

542 **Fig. 3. Self-assembling system reveals distinct organelle interactions and pathological signatures of**
543 **αSyn, Tau, and TDP-43 aggregates in human brain organoids.**
544
545 **(A)** Schematic of generating human cortical organoids from hESCs. **(B)** Immunostaining of fluorescently-
546 labeled PFFs or SAS3 (V5 tag) and pS129-αSyn in hESC-derived cortical organoids. Unlike PFFs, SAS3
547 can penetrate and induce PD-like pathology through the entire organoid. Scale bar equals 200 μm and 50
548 μm in enlargement. **(C)** Z-scanning confocal imaging of organoids stained for V5 tag and the mitochondrial
549 marker TOMM20. SAS3-induced aggregates colocalize with mitochondria (arrowhead), shown by XY
550 (main panel), XZ (bottom panel) and YZ (right panel) projections. Scale bar equals 10 μm. **(D-F)** Organoids
551 stained for ubiquitin and p62/SQSTM1 or with Nile red reveal that SAS3-induced aggregates are complex
552 inclusions containing αSyn and other proteins, similar to LBs found in human PD patients. **(D)** Ubiquitin
553 staining confirms that proteins in SAS3-induced aggregates are highly ubiquitinated. **(E)** Accumulation of
554 p62 in and around the aggregates indicates elevated autophagy. **(F)** Nile red staining demonstrates
555 enrichment of lipids in SAS-induced aggregates. **(G)** Mitochondrial marker TOMM20 accumulates
556 surrounding SA-Tau aggregates (arrowhead). **(H-I)** SA-Tau-induced aggregates are highly ubiquitinated
557 (**H**) and co-localize with neurofilament light chain (NfL) (**I**). **(J)** In contrast, SA-TDP-induced aggregates
558 show little to no co-localization with mitochondria (arrowhead), indicating a distinct aggregate composition
559 compared to SAS and SA-Tau. **(K)** Schematic comparison of SAS, SA-Tau and SA-TDP aggregates,
560 highlighting differences in aggregate morphology, interaction patterns with organelles, and associated
561 neurotoxicity. Scale bar equals 5 μm in **D-J**.

Fig S3: Self-assembling system reveals distinct organelle interactions and pathological signatures of αSyn, Tau, and TDP-43 aggregates.

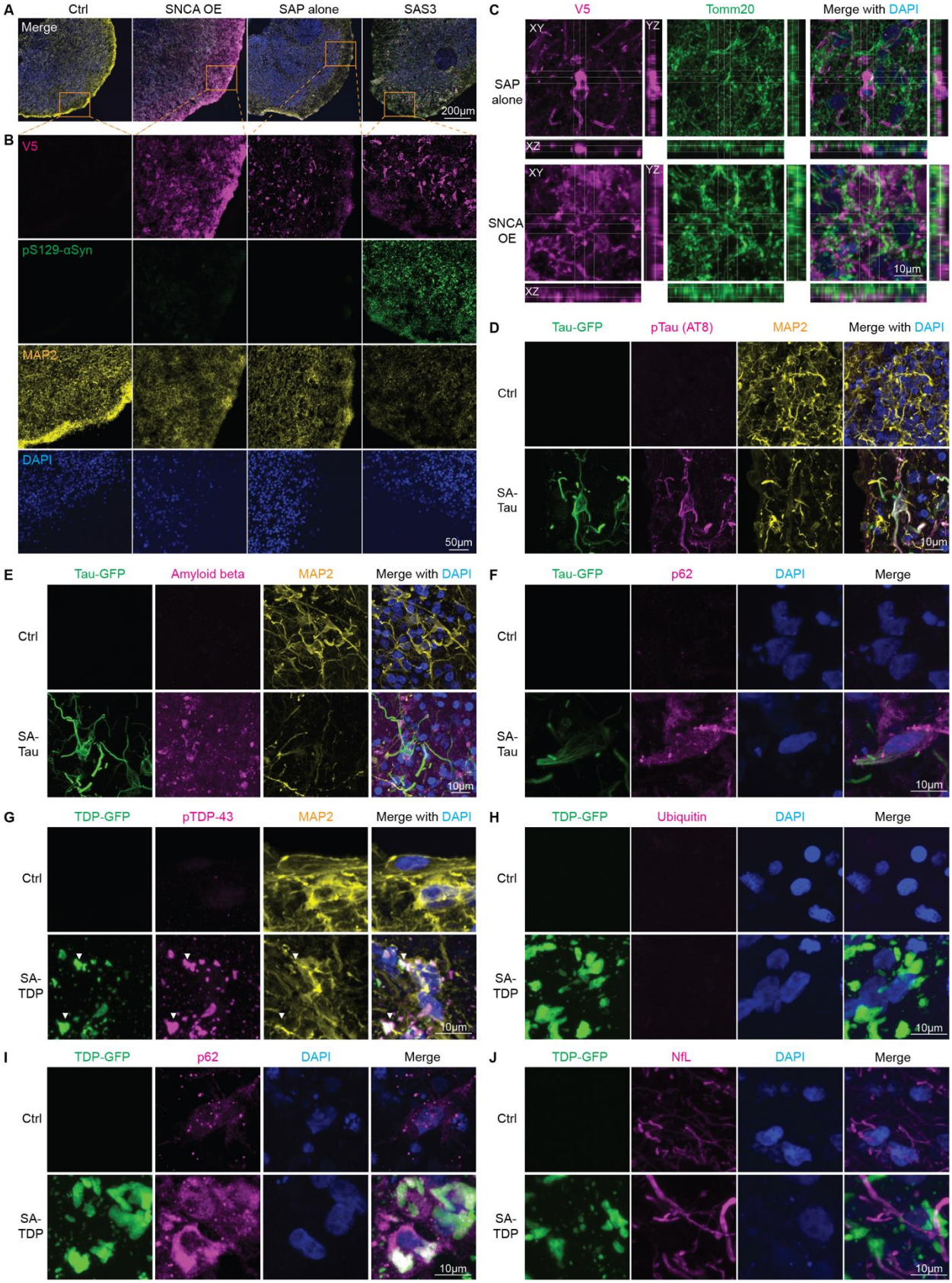

562

563 **Fig. S3. Self-assembling system reveals distinct organelle interactions and pathological signatures of**
564 **αSyn, Tau, and TDP-43 aggregates.**
565
566 **(A-B)** Immunostaining of V5 tag and pS129-αSyn in transduced human cortical organoids after 3 days of
567 dox treatment. Compared to *SNCA* OE and SAP alone, only SAS3 induces αSyn aggregation, intense αSyn
568 S129 phosphorylation, and neuron degeneration. Scale bar equals 200 μm and 50 μm in enlargement. **(C)**
569 Z-stack scanning of organoids stained for V5 tag and the mitochondrial marker TOMM20, showing that
570 *SNCA* OE and SAP construct-produced proteins do not colocalize with mitochondria, shown by XY (main),
571 XZ (bottom panel) and YZ (right panel) projections. **(D)** Immunostaining of GFP, pTau (AT8 antibody),
572 and MAP2 in human brain organoids shows robust Tau aggregation and pTau, as well as severe neuron
573 degeneration. **(E)** Immunostaining for amyloid beta in human brain organoids expressing SA-Tau reveals
574 Tau tangles promote the production of extracellular amyloid beta. **(F)** SA-Tau expressing cells exhibited
575 elevated accumulation of p62 signal. **(G)** Representative images of human brain organoids expressing SA-
576 TDP show cytoplasmic TDP-43 inclusions with strong pTDP-43 (arrowheads). Compared with SAS and
577 SA-Tau, human brain organoids expressing SA-TDP only shows mild neurodegeneration indicated by
578 MAP2 staining. **(H)** Ubiquitin staining shows SA-TDP-induced aggregates are not ubiquitinated, unlike
579 αSyn or Tau aggregates. **(I)** Accumulation of p62 in SA-TDP expressing cells indicates elevated autophagy.
580 **(J)** SA-TDP-induced aggregates do not colocalize with neurofilament light chain (NfL). Scale bar equals
581 10 μm in **B-J**.

Fig 4: SAS forms LB-like inclusions and nucleate aggregation of endogenous αSyn, triggering neuronal inflammation and death.

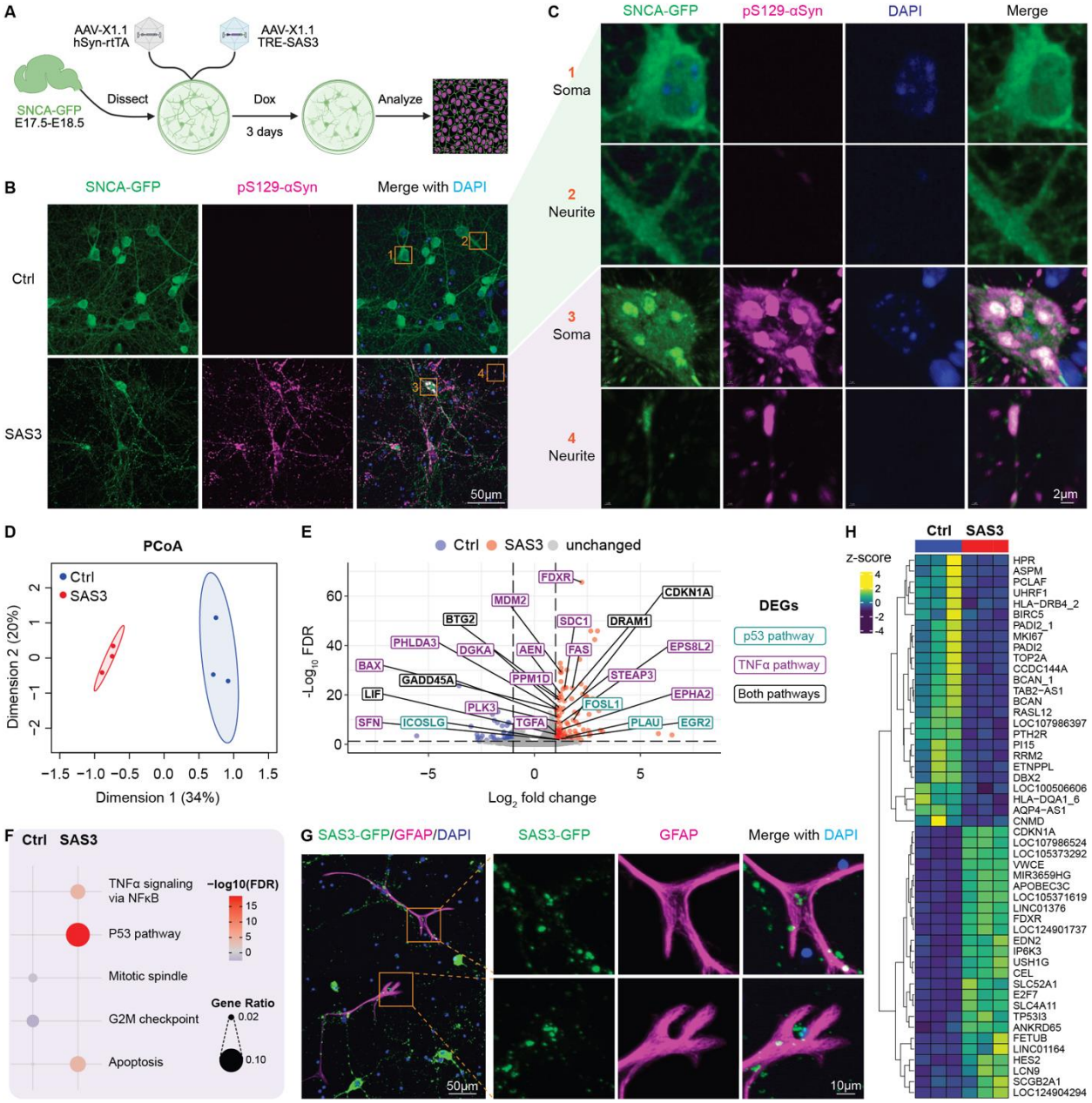

582

583 **Fig. 4. SAS forms LB-like inclusions and nucleate aggregation of endogenous αSyn, triggering**
584 **neuronal inflammation and death.**

585 **(A)** Experimental design for testing whether SAS3 can nucleate secondary aggregation of endogenous αSyn
586 in primary neurons carrying the SNCA-GFP reporter. **(B-C)** Immunostaining after 36 hours of dox
587 treatment shows SAS3-induced aggregates contain endogenous αSyn, as indicated by GFP signal. Scale
588 bar equals 50 µm in (**B**) and 2 µm in (**C**). **(D)** Principal coordinate analysis (PCoA) shows a clear separation
589 of transcriptomic profiles of SAS3 organoids transduced with hSyn-rtTA and TRE-SAS3 using AAV9-
590 X1.1 and control organoids transduced with only hSyn-rtTA. n= 3 biological replicates. **(E)** Volcano plot
591 of DEGs with FDR < 0.05 and $|\log_2$ fold change (FC)$|$ > 1. Genes belonging to the TNFα pathway are
592 highlighted in magenta, p53 pathway in cyan, and both in black. **(F)** Pathway analysis reveals that SAS3-
593 treated organoids contain significantly upregulated Gene Ontology (GO) pathways associated with
594 apoptosis and inflammation. **(G)** Immunostaining for the astrocyte marker GFAP reveals astrocyte
595 activation surrounding SAS3-expressing neurons and active engagement with protein inclusions. Scale bar
596 equals 50 µm in overview and 10 µm in enlargement. **(H)** Top 25 up- and downregulated genes.

Fig S4: SAS forms LB-like inclusions and nucleates aggregation of endogenous αSyn, triggering neuronal inflammation and death.

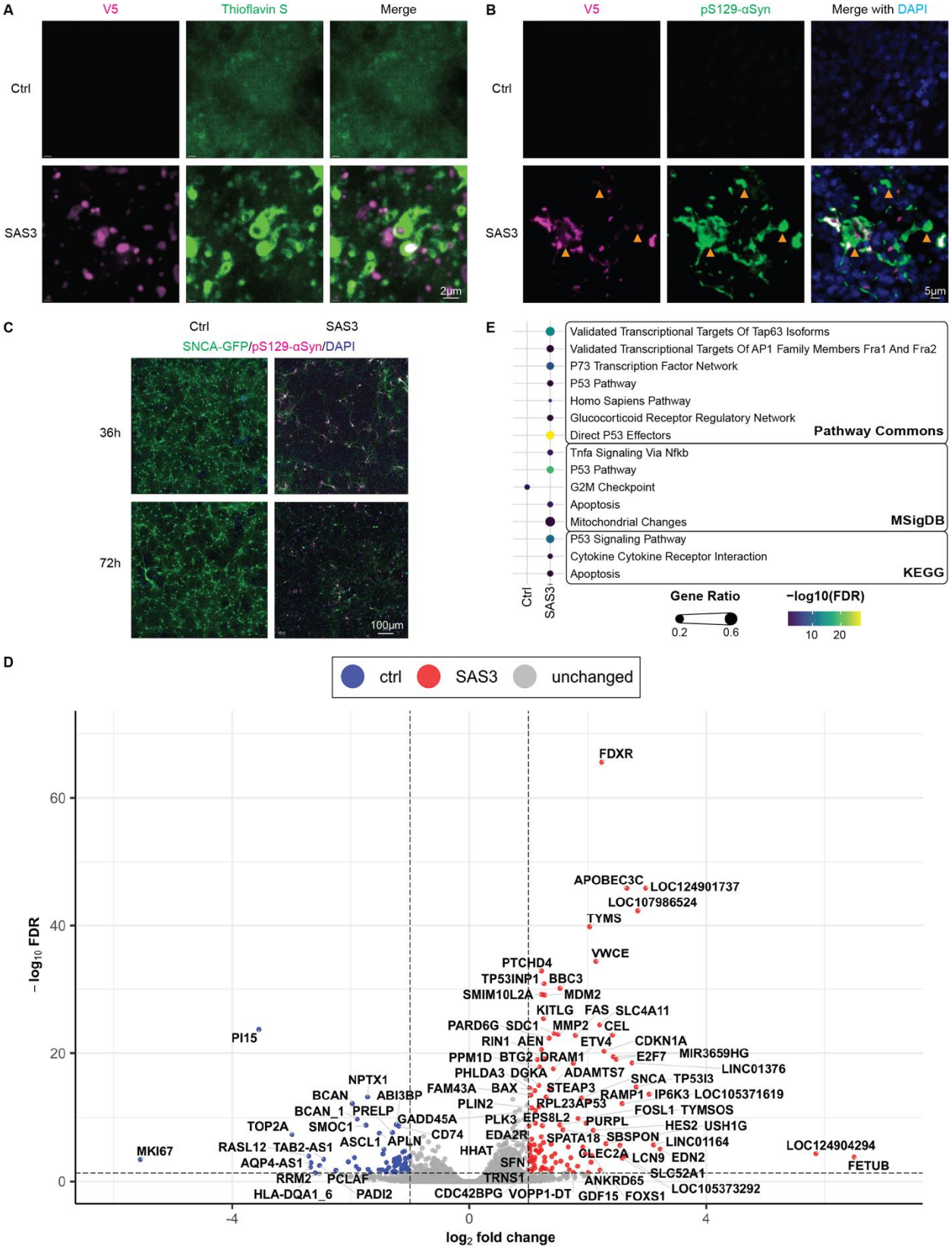

597

598 **Fig. S4. SAS forms LB-like inclusions and nucleates aggregation of endogenous αSyn, triggering**
599 **neuronal inflammation and death.**

600 **(A)** Organoids stained with thioflavin S demonstrate the presence of β-sheet structures within and around
601 SAS-induced aggregates. Scale bar equals 2 μm. **(B)** Organoids stained for V5 tag and pS129-αSyn reveals
602 the presence of V5-negative and pS129-αSyn-positive aggregates (arrowheads), indicating the formation
603 of endogenous αSyn aggregates. Scale bar equals 5 μm. **(C)** Immunostaining after 36 and 72 hours of dox
604 treatment indicates that neurons expressing SAS3 display degeneration at 36 hours which further worsens
605 by 72 hours. Scale bar equals 100 μm. **(D)** Volcano plot of transcriptomic data labeling all DEGs with FDR
606 < 0.05 and $|\log2$ fold change (FC)$| > 1$. Genes upregulated in SAS-treated organoids are shown in red and
607 those downregulated in blue. **(E)** Pathway analysis of DEGs using different databases reveals that SAS3-
608 treated organoids are characterized by significant up-regulation of pathways associated with apoptosis,
609 inflammation, and mitochondrial changes.

Fig 5: SAS induces PD-relevant histopathology and behavioral deficits in mice.

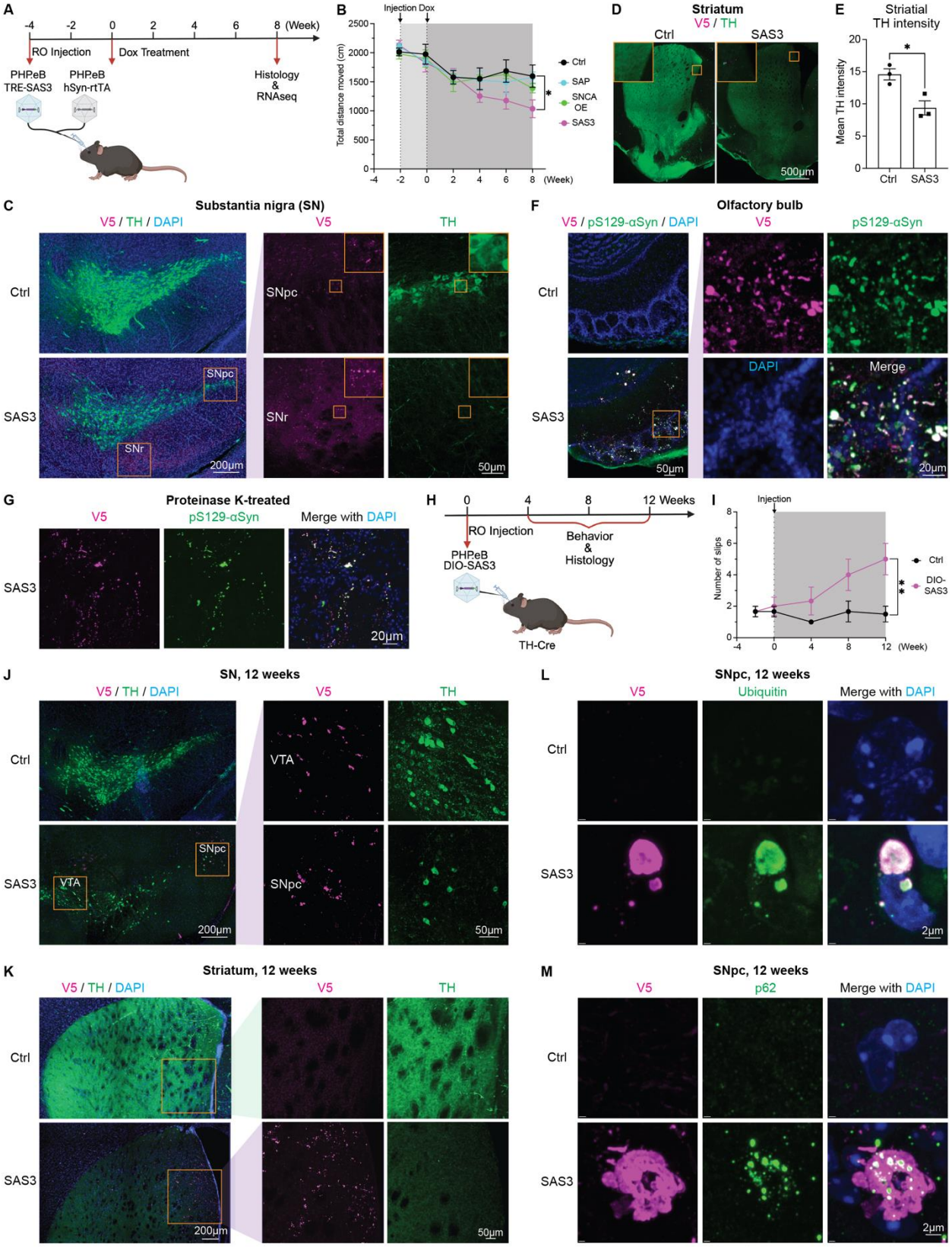

610

611 **Fig. 5. SAS induces PD-relevant histopathology and behavioral deficits in mice.**

612 **(A)** Experimental design for brain-wide delivery of SAS3 in WT C57BL/6J mice through retro-orbital (RO)
613 injection of AAV-PHP.eB. Behavioral assays were performed every other week and histology at week 8.
614 **(B)** After 4 weeks of dox treatment, SAS3-treated mice exhibited progressively decreased movement in the
615 open field test compared with other groups. n=5 mice per group. **(C)** Immunostaining of the V5 tag and TH
616 in the substantia nigra, showing aggregates in both the substantia nigra pars compacta (SNpc) and substantia
617 nigra reticulata (SNr), and a decreased number of TH+ neurons in the SNpc. Scale bar equals 200 μm and
618 50 μm in enlargements. **(D)** Representative images of dopaminergic neuron projections into the striatum.
619 Scale bar equals 500 μm. **(E)** Quantification of striatal TH intensity. n=3 mice. **(F)** Immunostaining of the
620 V5 tag and pS129-αSyn in the olfactory bulb, showing aggregates and strong αSyn phosphorylation. Scale
621 bar equals 50 μm and 20 μm in enlargement. **(G)** Immunostaining for the V5 tag and pS129-αSyn in the
622 olfactory bulb of SAS3-treated mice after proteinase K treatment, showing resistance of aggregates to
623 degradation. Scale bar equals 20 μm. **(H)** Experimental design for selectively delivering SAS3 into
624 dopaminergic neurons. Cre-dependent SAS3 (DIO-SAS3) was RO injected into TH-Cre mice using AAV-
625 PHP.eB. Behavioral assays and histology were performed at 4, 8, and 12 weeks. **(I)** After 4 weeks of dox
626 treatment, SAS3-treated mice exhibited significant motor impairments in the beam crossing assay,
627 displaying more slips than controls. n=5 mice per group. **(J)** Immunostaining of the V5 tag and TH in the
628 substantia nigra (SN) region, with enlarged images of the ventral tegmental area (VTA) and SNpc. **(K)**
629 Immunostaining of the V5 tag and TH in the striatum, suggesting progressive accumulation of aggregates
630 and potential spreading along the nigrostriatal pathway. Scale bar equals 200 μm and 50 μm in enlargements
631 in **J**, **K**. **(L-M)** Immunostaining of ubiquitin **(L)** and p62/SQSTM1 **(M)** confirms that SAS3-induced
632 aggregates are similar to LBs both in morphology and composition. Scale bars equal 2 μm. Data are
633 presented as mean ± SEM; statistical analysis was performed using the ANNOVA with multiple
634 comparison correction post-hoc tests in (**B**) and unpaired t test in (**E&I**); *$p<0.05$, **$p<0.01$.

Fig S5: Systemic delivery of SAS induces PD-relevant histopathology.

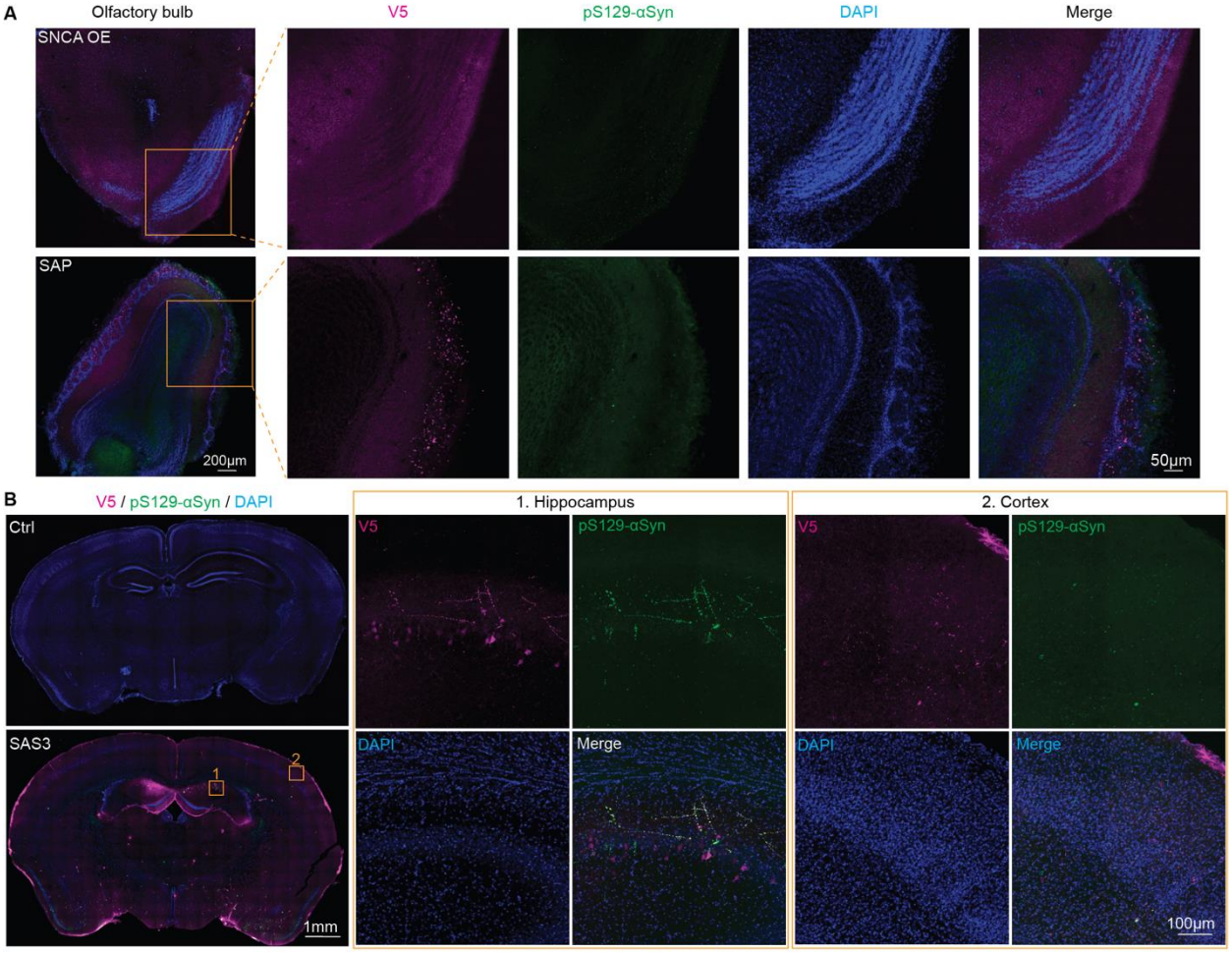

635

636 **Fig. S5. Systemic delivery of SAS induces PD-relevant histopathology.**

637 **(A)** Immunostaining for the V5 tag and pS129-αSyn in the olfactory bulb of C57BL/6J mice, showing that
638 *SNCA* OE and SAP-alone constructs do not induce strong αSyn phosphorylation in olfactory bulb. Scale
639 bar equals 200 μm and 50 μm in enlargement. **(B)** Immunostaining for the V5 tag and pS129-αSyn in the
640 hippocampus and cortex of SAS3-treated or control mice, showing aggregates and strong αSyn
641 phosphorylation in neurons induced by SAS3. Scale bar equals 1 mm and 100 μm in enlargement.

642

Fig S6: Dopaminergic neuron-targeted SAS recapitulates PD progression.

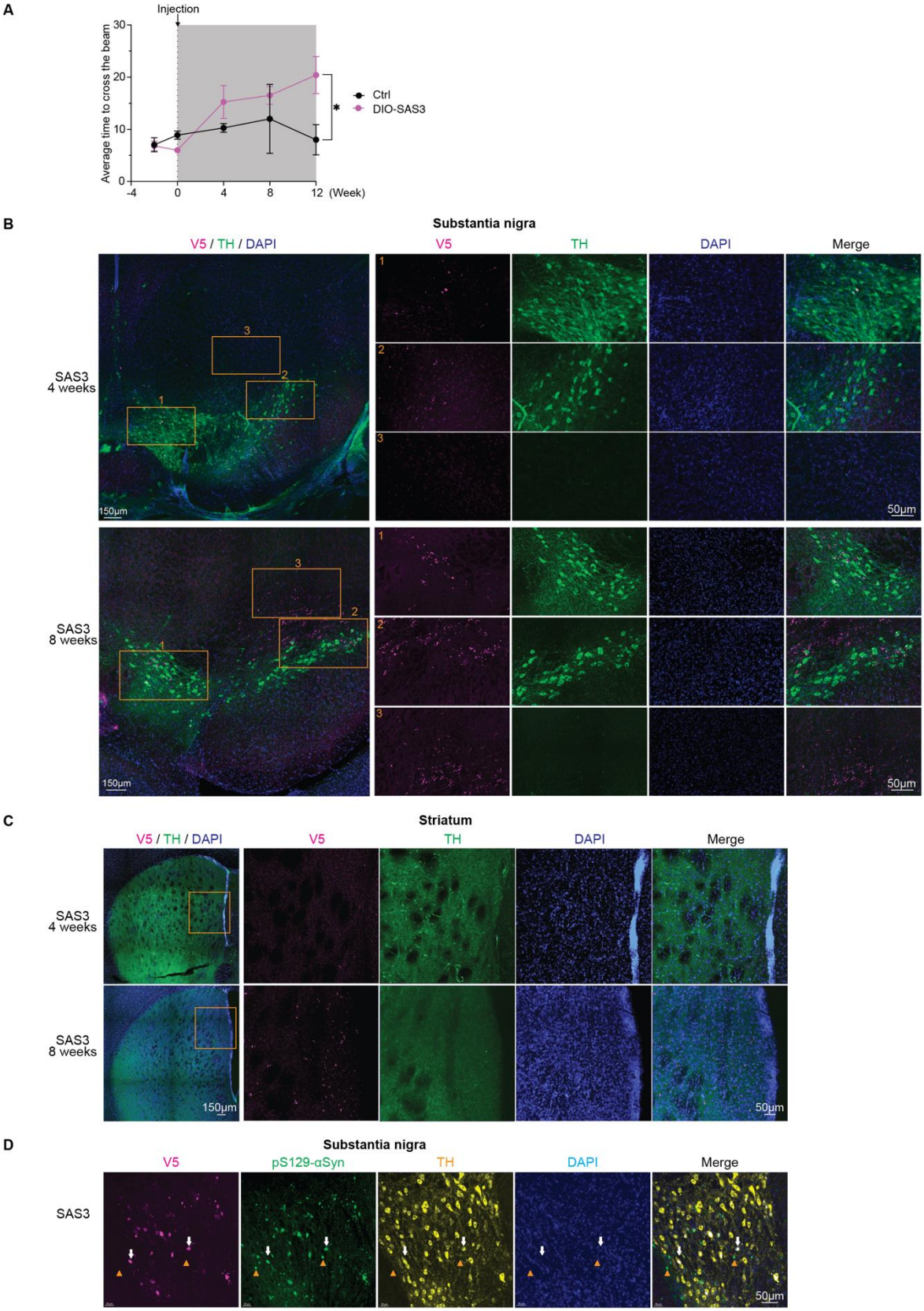

643

644 **Fig. S6. Dopaminergic neuron-targeted SAS recapitulates PD progression.**

645 **(A)** After 4 weeks of dox treatment, DA neuron-targeted SAS3 mice exhibited significant motor
646 impairments in the beam crossing assay, requiring more time to cross the beam. **(B)** Immunostaining for
647 the V5 tag and TH in the SN region of SAS3-treated TH-Cre mice at 4 weeks and 8 weeks, with enlarged
648 images of the ventral tegmental area (VTA, area 1), SNpc (area 2), and non-TH+ region (area 3). Scale bars
649 equal 150 μm and 50 μm in enlargements. **(C)** Immunostaining for the V5 tag and TH in the striatum of
650 SAS3-treated TH-Cre mice at 4 weeks and 8 weeks, indicating progressive aggregate accumulation and
651 potential spreading along the nigrostriatal pathway. Scale bar equals 150 μm and 50 μm in enlargement. **(D)**
652 Immunostaining for V5, pS129-αSyn, and TH in the SNpc reveals that not only SAS3-expressed proteins
653 (arrows) but also endogenous αsyn (arrowheads) formed aggregates and became phosphorylated. Scale bar
654 equals 50 μm. Data are presented as mean ± SEM; statistical analysis was performed using unpaired t test;
655 *$p<0.05$.

656

657

658

Fig 6: SAS activates microglia and triggers immune response in mice.

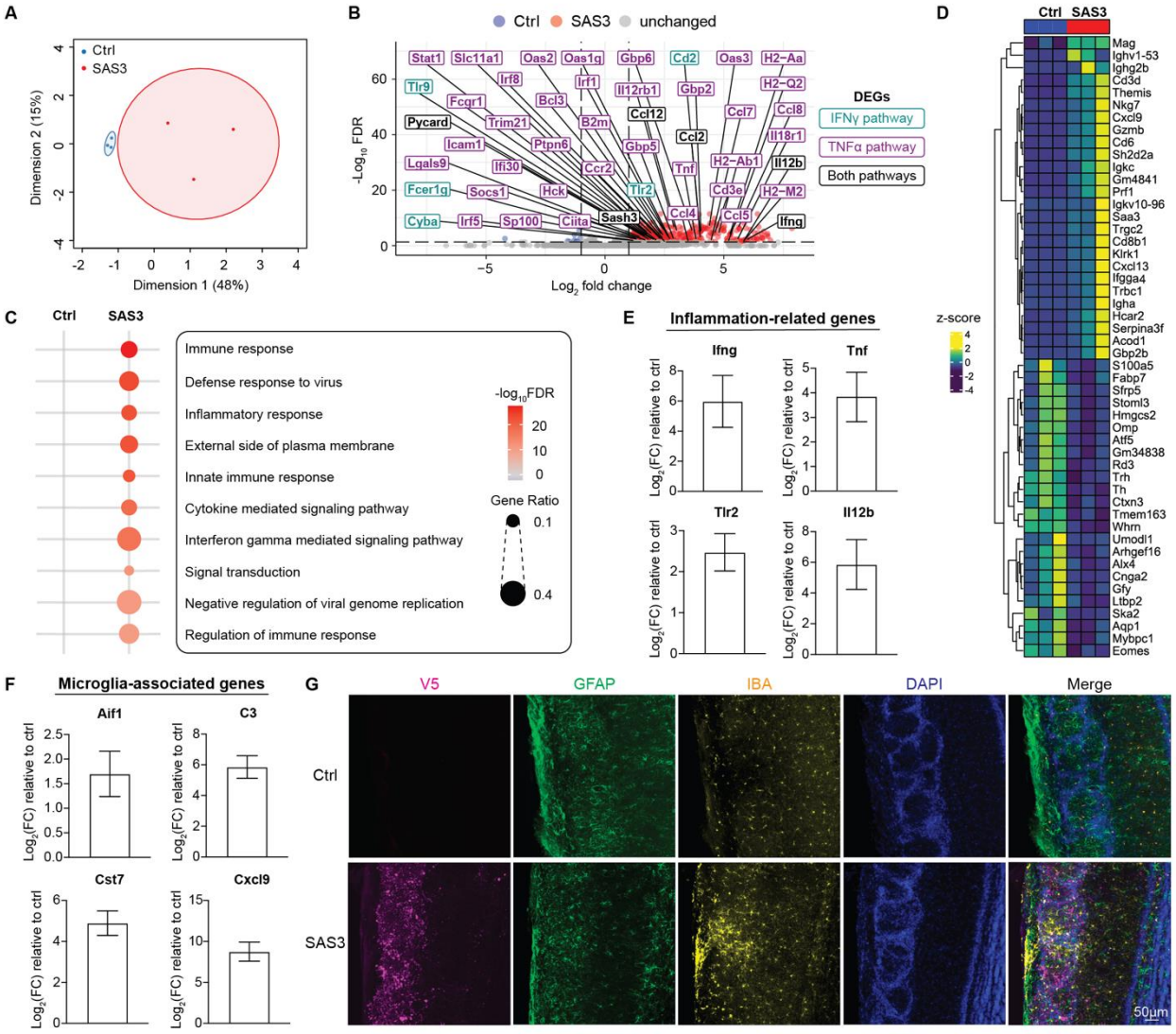

659

660 **Fig 6: SAS activates microglia and triggers immune response in mice.**

661 **(A)** PCoA of transcriptomic data shows separation between SAS3-treated mice (transduced with hSyn-rtTA
662 and TRE-SAS3 using AAV-PHP.eB) and controls (transduced with only hSyn-rtTA). n=3 biological
663 replicates. **(B)** Volcano plot of DEGs with FDR < 0.05 and $|\log_2$ fold change (FC)$|$ > 1. Genes belonging to
664 the TNFα pathway are highlighted in magenta, IFN-γ pathway in cyan, and both in black. **(C)** Top 10
665 significantly altered GO pathways in SAS3-transduced mice indicate upregulation of pathways involved in
666 inflammation. **(D)** Top 25 up- and downregulated genes. **(E)** Quantification of upregulation of
667 representative genes of the inflammation-related IFN-γ, TNF-α, TLR, and interleukin pathways in SAS3-
668 treated mice compared to controls. **(F)** Quantification of upregulation of representative genes involved in
669 microglia activation. **(G)** Immunostaining of GFAP and IBA1 in the olfactory bulb, showing activated
670 microglia clustered around SAS-induced aggregates. Scale bar equals 50 μm. Data are present as mean ±
671 SEM.

Fig S7: SAS activates microglia and triggers immune response in mice.

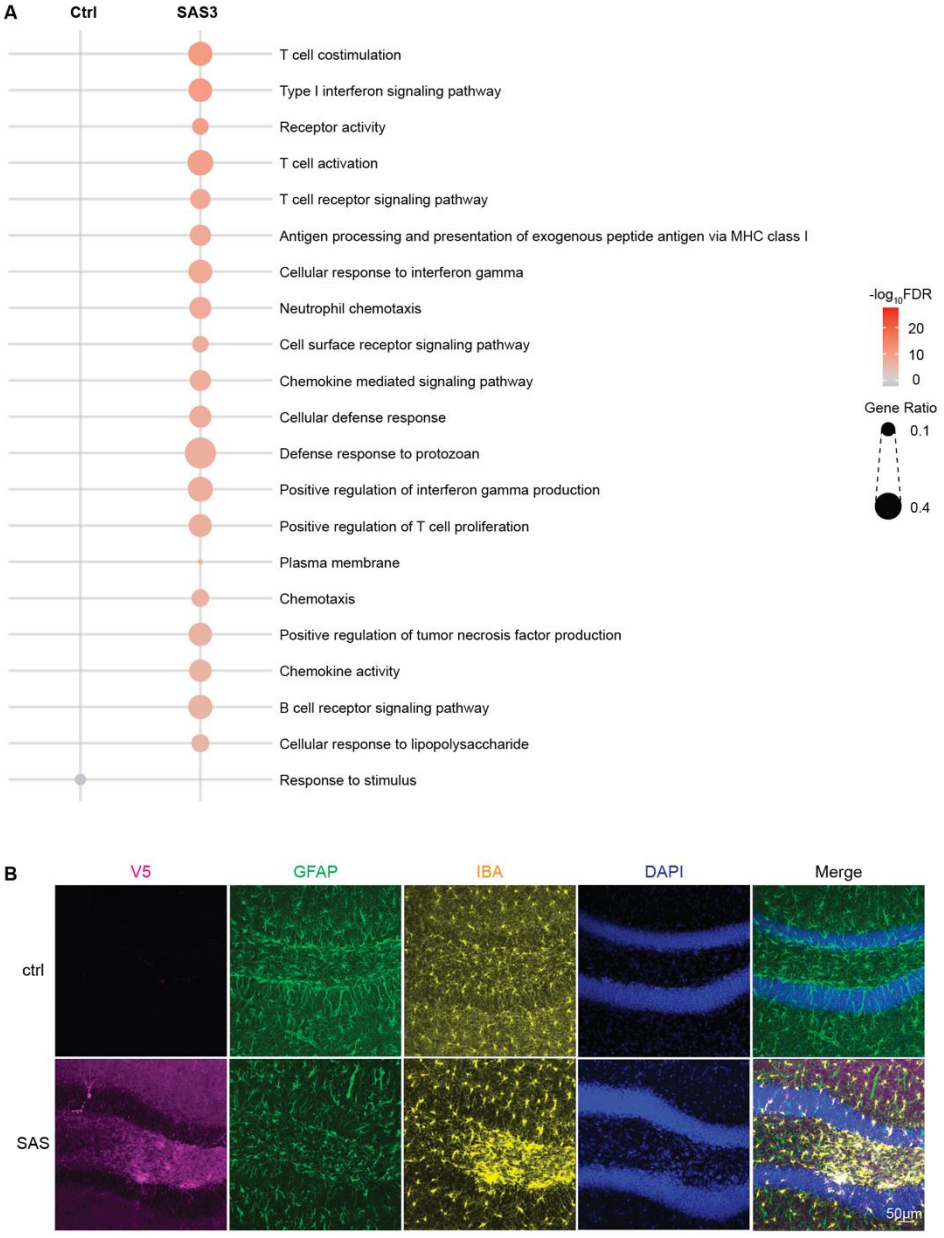

672

673 **Fig. S7. SAS activates microglia and triggers immune response in mice.**

674 **(A)** Most significantly differentially regulated GO pathways, revealing that SAS3-transduced mice show
675 significant up-regulation of pathways associated with inflammation and immune response. **(B)**
676 Immunostaining for GFAP and IBA1 in the hippocampus, showing activated microglia clustered around
677 SAS-induced aggregates. Scale bar equals 50 μm.

678 **STAR Methods**

679 ***Key resources table (Table S4)***

680

681 ***Animals***

682 Animal husbandry and experimental procedures involving mice were done in accordance with
683 protocols approved by the California Institute of Technology Institutional Animal Care and Use
684 Committee (IACUC, protocol 1650) and the mice were handled in accordance with the principles
685 and procedures of the Guide for the Care and Use of Laboratory Animals of the National Institutes
686 of Health. Mice were group housed at 2-3 mice per cage with 13/11 light/dark cycles at ambient
687 temperatures of 71–75°F and 30–70% humidity. C57BL/6J (Jackson Labs #026267), $Snca^{tm1.1Kluk/J}$
688 (Jackson Labs #035412) and heterozygous B6.Cg-7630403G23$Rik^{Tg(Th\text{-}cre)1Tmd/J}$ (Jackson Labs
689 #008601) mice were used in experiments. Genotyping was performed by Transnetyx. AAVs were
690 administered via retro-orbital injection during isoflurane anesthesia (1-3% in 95% O2/5% CO2,
691 provided by nose cone at 1 L/min), at 1×10^{12} viral genomes (v.g.) per animal. A detailed protocol
692 for systemic AAV administration through retro-orbital injection is available on protocols.io
693 (dx.doi.org/10.17504/protocols.io.36wgqnw73gk5/v1). Mice were randomly assigned to different
694 conditions.

695

696 ***Cell lines***

697 HEK 293 cells (ATCC, CRL-3216) were used in SAS screening and characterization. The human
698 embryonic stem cell line (hESC) line CSES07 (Cedars Sinai, CVCL_B818) was used to derive
699 both monolayer neurons and organoids. CSES07 was obtained from Cedars Sinai Medical Center
700 with a verified normal karyotype and was contamination-free. All cell lines were authorized for
701 use under the supervision of the California Institute of Technology Institutional Biosafety
702 Committee (IBC #22-182).

703

704 ***SAS library, SA-Tau and SA-TDP design***

705 To investigate whether intracellular αSyn aggregation can recapitulate Parkinsonian pathology, we
706 designed a library of self-assembling synuclein (SAS) constructs. Each construct consisted of wild-
707 type (WT) αSyn (UniProt ID: P37840-1) fused to selected self-assembling proteins (SAPs). SAPs
708 were chosen based on structural evidence indicating terminal accessibility and the nature of their
709 assemblies, as revealed by structural studies. 1POK(E239Y)[24], DHF40, and DHF46[22] were
710 selected based on known filament formation (PDB entries 5LP3 and 6E9R), while 2VYC (K491L,
711 D494L, D497L)[47] and gamma-prefoldin (γPFD)[25] were selected for their punctate assembly
712 characteristics (PDB entry 6VY1). Additionally, cytoskeletal proteins β-tubulin (PDB: 3J2U) and
713 β-actin (PDB: 6DJO) were included to evaluate intracellular fiber-mediated effects. Several
714 constructs also integrated mitochondrial targeting proteins (TOMM5, TOMM20) to explore how
715 spatial localization influences aggregation outcomes. All fusion junctions incorporated flexible
716 glycine-rich linkers (GGSGGTGG) and V5 epitope tags for enhanced detection and
717 characterization. SA-Tau and SA-TDP construct consisted of human Tau (isoform 2N4R) or TDP-

718 43 fused with 1POK(E239Y). Detailed information on SAS, SA-Tau and SA-TDP constructs is
719 listed in Supplemental Table 1.
720
721 ***SAS screening in HEK cells***
722 SAS plasmids were transfected into HEK cells using Lipofectamine 3000 (ThermoFisher,
723 L3000008) following the manufacturer's instructions. Briefly, 100K HEK cells were plated in 24-
724 well plates. The next day, 0.4 µg SAS plasmids and 0.1 µg rtTA plasmids were transfected into
725 each well. Cells were incubated with lipofectamine overnight. The medium was switched to 5%
726 FBS in DMEM/F12 the next morning, and 10 µg/mL of doxycycline (Sigma, Cat # D9891-10G)
727 was added into the medium. After 3 days of doxycycline treatment, cells were fixed and stained.
728 For protocol, see **dx.doi.org/10.17504/protocols.io.6qpvr97wzvmk/v1**
729
730 ***Immunostaining of cultured cells***
731 At predetermined time points, cells were removed from the incubator, washed once with
732 phosphate-buffered saline (PBS), and fixed with 4% paraformaldehyde for 10 minutes at room
733 temperature (RT). After washing 3 times with PBS, the blocking buffer containing 1xPBS, 0.03%
734 Triton X-100 (PBST), and 5% normal donkey serum was applied and incubated at RT for 60
735 minutes. Primary antibodies were diluted in fresh blocking buffer, added on the cell, and incubated
736 overnight at 4°C. The next day, the antibody solution was washed off with PBST for 10 minutes,
737 3 times. Secondary antibodies were applied for 60 minutes and then washed off with PBST for 10
738 minutes, 3 times. After the final wash, cells remain in PBST for imaging. Antibodies and reagents
739 used were listed in the key resource table.
740 For protocol, see **dx.doi.org/10.17504/protocols.io.4r3l29eb4v1y/v1**
741
742 ***Western blotting***
743 Western blotting was performed using the iBind Automated Western System following the
744 manufacturer's instructions. Briefly, cells were collected with cold DPBS and lysed with RIPA
745 buffer. Total protein concentration was measured using Qubit Protein BR Assay kit and Qubit4.
746 An equal amount of protein was run in Bio-Rad 4-20% TGX stain-free gels and then transferred
747 to a PVDF membrane. Membranes were fixed with 4% paraformaldehyde for 10 minutes before
748 blotting. Protein immunodetection was performed with indicated antibodies using the iBind
749 Automated Western System. Signals were detected with Max Western ECL and imaged with a
750 ChemiDoc imaging system. Antibody information and reagents used are listed in the key resource
751 table (**Table S4**).
752 For protocol, see **dx.doi.org/10.17504/protocols.io.j8nlk96p6v5r/v2**
753
754 ***Viral vector production***
755 AAV packaging and purification were carried out as previously described[48]. The viruses for *in*
756 *vitro* experiments were produced by suspension HEK cells. In brief, recombinant AAV was
757 produced by triple transfection of cells in suspension using the VirusGEN AAV Kit with RevIT

758 enhancer (Mirus Bio, MIR 8007) at a molar ratio of transgene: AAV capsid: pHelper = 1:2:0.5, as
759 per the manufacturer's instructions. The total DNA amount was 2 µg per mL of cells. Virus-
760 producing cells and medium were harvested 72 hours post-transfection. The viruses used in animal
761 experiments were produced by adherent HEK cells. In brief, HEK cells are transiently transfected
762 using polyethyleneimine (PEI) at a molar ratio of transgene: AAV capsid: pHelper = 1:4:2. 120
763 hours after transfection, the producer cells were harvested, and cell culture media was collected at
764 72- and 120-hours post-transfection. Following cell lysis and nuclease digestion, viruses from
765 suspension cells and adherent cells were purified using iodixanol step gradient columns followed
766 by ultracentrifugation, as previously detailed[48]. The purified AAVs were quantified through
767 droplet digital PCR (ddPCR) following Addgene's protocol with modifications[49]. Briefly, AAV
768 samples were first serially diluted to achieve a suitable concentration for ddPCR analysis. The
769 PCR reaction mixture was prepared using ddPCR EvaGreen Supermix (Bio-Rad), primers for
770 WPRE or ITRs, the diluted AAV sample, and nuclease-free water. The mixture was then
771 partitioned into droplets using the QX200 Droplet Generator, and the droplets were transferred to
772 a 96-well plate for PCR in a thermocycler. After cycling, the droplets were read using a QX200
773 Droplet Reader, and the concentration of the viral genome was analyzed using QuantaSoft
774 software. The viral genome titer in original sample was then back calculated using the dilution
775 factors. The final viral preparation was stored in DPBS with Pluronic F-68 to prevent adhesion
776 loss. The reagents used are listed in the key resource table (**Table S4**).
777 For protocol, see **dx.doi.org/10.17504/protocols.io.ewov1dpeovr2/v1**
778
779 ***Primary neuron preparation***
780 The day before the procedure, 10× HBSS (Thermo Fisher, Cat # 14065056) was diluted to 1×
781 using sterile distilled water (Invitrogen, Cat # 10977015) and pre-cooled to 4°C. Glass inserts
782 (Neuvitro Corporation, Cat # GG-12-15 Pre) were placed in 24-well plates and were coated with
783 Poly-D-lysine (Millipore Sigma, Cat # A-003-E) overnight. Plating media was prepared using the
784 BrainPhys Neuronal Medium SM1 Kit (Stem Cell Technologies, Cat # 05792), 1× Glutamax,
785 (Thermo Fisher,Cat # 35050061), 1× Penicillin-Streptomycin (Thermo Fisher, Cat # 15140122,),
786 and 1× l-glutamine (Bio-Techne, Cat # 0218). Pregnant mice from JAX were euthanized on day
787 17 of pregnancy. Embryos were removed, decapitated, and brains were isolated in cold HBSS.
788 Cortices and hippocampi were dissected, and hippocampi were quartered and placed into 15 mL
789 tubes. Papain (Sigma Aldrich, Cat # P3125-250MG) was added for digestion, followed by washing
790 with a stopping medium containing HBSS 1× and 10% Fetal Bovine Serum. Hippocampi were
791 dissociated by gentle pipetting, and supernatants with dissociated neurons were collected. After
792 centrifugation, cells were resuspended in plating media, counted, and seeded at 200,000 cells/well
793 on Poly-D-lysine-coated inserts. After 72 hours, the media was replaced with a combination of
794 500 mL Neurobasal Medium (Thermo Fisher, Cat # 21103049), 2 mL B27 Supplement (Thermo
795 Fisher, Cat # 17504044), and 0.5 mM L-glutamine (Bio-Techne, Cat # 0218). Virus was then
796 added for indicated times and doses.
797 For protocol, see http://dx.doi.org/10.17504/protocols.io.5qpvo98ozv4o/v1 .

798
799 ***Cortical neurons and organoid differentiation***
800 hESCs were plated on 6-well plates coated with Vitronectin (Gibco, Cat # A14700) at 1:100 diluted
801 in DPBS (Gibco, Cat #14190250) and maintained in E8 medium (Thermo Fisher, Cat #A1517001).
802 The E8 medium was changed every day, and the cells were passaged every 3-5 days at 70-85%
803 confluence. The cells were passaged using EDTA dissociation as described previously[50]. To
804 induce differentiation, hESCs were dissociated at 70%-80% confluence using EDTA dissociation
805 buffer and replated as a single cell suspension on Matrigel-coated 24-well plates at a density of
806 100K cells/cm^2 in E6 medium (Thermo Fisher, Cat #A1516401) containing 10 μM ROCK-
807 inhibitor (Y-27632; R&D, Cat #1254). The cells were kept in E6 medium + Y-27632 overnight.
808 The next day, the medium was switched to a neuroectoderm-inducing medium. The cells were
809 kept in E6 medium containing 10 μM SB431542 (R&D, Cat #1614), 100 nM LDN139189 (R&D,
810 Cat #6053), and 500 nM XAV (R&D, 3748) for the first 4 days and then switched to E6 medium
811 containing 10 μM SB and 100 nM LDN for 6 days. Then the cells were switched to progenitor
812 expanding medium, containing neurobasal (NB) medium supplemented with l-glutamine (Gibco,
813 Cat #25030-164), N2 (Stem Cell Technologies, 07156), B27 (Life Technologies, Cat #17504044)
814 and NEAA (Sigma, Cat #M7145) for 10 days. At D20, the neuron progenitors were dissociated
815 into single cells and replated in a V-bottom ultra-low attachment 96-well plate at 100K per well to
816 form neuron spheres. After 4 days, the spheres were transformed to low attachment 10 cm dishes
817 and placed on a shaker for long-term culture and maturation in cortical neuron medium containing
818 NB/N2/B27/Glu/NEAA, ascorbic acid (200 μM, Sigma, 4034-100g), dbcAMP (500 μM, Sigma,
819 Cat #D0627), BDNF (20 ng/mL, R&D, Cat #248-BDB) and GDNF (20 ng/mL, Peprotech, Cat
820 #450-10)[51]. Organoids were cultured in suspension for 90 days before adding viruses.
821 For protocol, see **dx.doi.org/10.17504/protocols.io.3byl4wrzovo5/v1**
822
823 ***Open field test (OFT)***
824 Mice were tested in the OFT bi-weekly. The open-field apparatus consisted of four square arenas
825 (27 cm × 27 cm), with a camera (EverFocus, EQ700) placed 1.83 m above the floor of the arenas.
826 EthoVision XT was used to capture and subsequently analyze animal locomotion. Each trial
827 consisted of a 2 min habituation period, followed by a 10 min test period. To avoid confounds due
828 to odors from non-cagemates, only animals from the same cage were recorded simultaneously.
829 Behavior equipment was disinfected and deodorized between each animal. The distance traveled
830 over the course of the experimental period was determined.
831 For protocol, see **dx.doi.org/10.17504/protocols.io.5qpvo972xv4o/v1**
832
833 ***Beam crossing assay***
834 To measure skilled locomotion using the narrowing beam assay, a clear plexiglass beam consisting
835 of three 25 cm segments (widths 3.5 cm, 2.5 cm, and 1.5 cm) was elevated above the table surface
836 using empty clean cages. At the narrow end, an empty cage was placed on its side, and bedding
837 from the animal's home cage was placed inside. A white light was also placed over the broad end

838 to motivate animals to move across the beam. For each trial, animals were placed at the end of the
839 widest segment, with all 4 limbs touching the beam surface. Each trial was recorded with a video
840 camera placed to the side and perpendicular to the beam's length, affording a view of both left and
841 right hindlimbs. A trial was considered complete once the animal had traversed the beam, without
842 turning around, and entered the goal cage. Once an animal had completed three trials, the session
843 was completed. Beam crossing was analyzed using BORIS software, measuring the time taken to
844 cross the beam and the number of foot slips.
845 For protocol, see **dx.doi.org/10.17504/protocols.io.n92ldr2jxg5b/v1**
846
847 ***Tissue harvesting and processing***
848 Animals were transcardially perfused with 30 mL of ice-cold heparinized 1× PBS, and brains were
849 dissected. One hemisphere of the brain was used for RNAseq. For analysis of fluorescent protein
850 expression, one hemisphere of the brain was submerged in ice-cold 4% PFA formulated in 1× PBS
851 and fixed for 24-48 hr at 4°C. Brains were subsequently cryoprotected at 4°C in a solution
852 containing 30% (w/v) sucrose for 72 hr. Brains were flash-frozen in O.C.T. Compound (Scigen,
853 Cat # 4586) using a dry ice-ethanol bath and kept at -80°C until sectioning.
854 For protocol, see **dx.doi.org/10.17504/protocols.io.ewov1d5xovr2/v1**.
855
856 ***Immunostaining of mouse tissue***
857 Brains were sliced at 100 µm using a cryostat (Leica Biosystems, CM1950) and collected in 1×
858 PBS. Sections were stored in PBS supplemented with 0.02% Azide.
859 For protocol, see **dx.doi.org/10.17504/protocols.io.x54v9rkzpv3e/v1**.
860 For immunostaining, brain sections were blocked with 5% normal donkey serum in 0.1 % PBST
861 for 90 mins, then incubated with primary antibody solution prepared in 0.1 % PBST supplemented
862 with 5% normal donkey serum overnight on a shaker at 4°C. After washing in 0.1 % PBST (3 ×
863 30 min), the sections were incubated with secondary antibodies overnight on a shaker at 4°C and
864 then washed 3 x 30 min in 0.1 % PBST. The tissues were mounted on glass slides with Prolong
865 Diamond Antifade mounting media (Thermo Fisher Scientific, Cat # P36970). Imaging was
866 performed with a spinning disk confocal microscope. Antibodies are listed in the Key Resource
867 Table (Table S4).
868 For protocol, see https://dx.doi.org/10.17504/protocols.io.kqdg3q7ypv25/v1
869
870 ***RNA extraction***
871 RNA extraction from cells was performed using the Direct-zol RNA Miniprep kit (Zymo, Cat #
872 R2051). Briefly, the cells were removed from incubator, washed once with DPBS, then 350 µL of
873 TRIzol was added directly to each well to collect the cells. Subsequent RNA extraction was done
874 following the manufacturer's instructions.
875 For protocol, see **dx.doi.org/10.17504/protocols.io.6qpvr9r2zvmk/v1**
876

877 RNA extraction from organoids was performed using the QIAshredder kit (Qiagen, Cat # 79654)
878 and miRNeasy Mini Kit (Qiagen Cat # 217004). Briefly, 3 organoids were harvested for each RNA
879 extraction and 350 µL of Buffer RLT from RNeasy Mini Kit + 3.5 µL β-mercaptoethanol were
880 added to lyse the organoid. Subsequent RNA extraction was done following the manufacturer's
881 instructions.
882 For protocol, see **dx.doi.org/10.17504/protocols.io.81wgbr95qlpk/v1**
883
884 RNA extraction from mouse brain tissue was performed using the miRNeasy Mini Kit (Qiagen
885 catalog, Cat # 217004) on a QIAcube Connect (Qiagen). After perfusion with cold PBS, the entire
886 olfactory bulb was dissected and placed in TRIzol directly and processed immediately for RNA
887 extraction following manufacturer's instructions.
888 For protocol, see **dx.doi.org/10.17504/protocols.io.eq2ly618pgx9/v1**.
889
890 ***RNA sequencing (RNA-seq)***
891 Bulk RNAseq was performed by the Millard and Muriel Jacobs Genetics and Genomics
892 Laboratory at the California Institute of Technology. RNA integrity was assessed using the RNA
893 6000 Pico Kit for Bioanalyzer (Agilent Technologies, Cat # 5067-1513), and mRNA was isolated
894 from ~1 µg of total RNA using the NEBNext Poly(A) mRNA Magnetic Isolation Module (NEB,
895 Cat #E7490). RNA-seq libraries were constructed using the NEBNext Ultra II RNA Library Prep
896 Kit for Illumina (NEB, Cat. No. / ID: E7770) following the manufacturer's protocols. Briefly,
897 mRNA was fragmented to an average size of 200 nt by incubating at 94°C for 15 min in the first
898 strand buffer. cDNA was then synthesized using random primers and ProtoScript II Reverse
899 Transcriptase followed by second strand synthesis using NEB Second Strand Synthesis Enzyme
900 Mix. The resulting DNA fragments were end-repaired, dA-tailed and ligated to NEBNext hairpin
901 adaptors (NEB, Cat. No. / ID: E7335). Following ligation, adaptors were converted to the "Y"
902 shape by treating with USER enzyme, and DNA fragments were size selected using Agencourt
903 AMPure XP beads (Beckman Coulter # A63880) to generate fragment sizes between 250-350 bp.
904 Adaptor-ligated DNA was PCR amplified followed by AMPure XP bead clean up. Libraries were
905 quantified using a Qubit dsDNA HS Kit (ThermoFisher Scientific, Cat. No. / ID: Q32854), and
906 the size distribution was confirmed using a High Sensitivity DNA Kit for Bioanalyzer (Agilent
907 Technologies, Cat. No. / ID: 5067- 4626). Libraries were sequenced on an Illumina NextSeq2000
908 in paired end mode with a read length of 50 nt and sequencing depth of 25 million reads per library.
909 Base calls and FASTQ generation were performed with DRAGEN 4.2.7.

910 ***Transcriptomics data analysis***
911 Raw sequencing reads were processed and aligned by Rsubread package v2.16.1
912 (https://bioconductor.org/packages/release/bioc/html/Rsubread.html, RRID:SCR_016945) in R
913 (v4.3.2) to align trimmed reads. For human cortical organoids, reads were aligned to the
914 GRCh38.p14 reference genome, while mouse brain tissues were aligned to the GRCm39 reference
915 genome. The corresponding gene annotation files (GTF) were used with featureCounts
916 (https://subread.sourceforge.net/featureCounts.html, RRID:SCR_012919) to generate gene level

counts for each dataset. Data were subsequently normalized with DESeq2 v1.42.1 (https://bioconductor.org/packages/release/bioc/html/DESeq2.html, RRID:SCR_015687) and principal coordinate analysis was subsequently performed by multidimensional scaling to assess sample level clustering using the limma package (v3.60.4, RRID:SCR_010943). DESeq2 was then used to assess differential gene expression between rtTA and SAS3 samples. A two-tailed false discovery rate (FDR) < 0.05 (original Benjamini-Hochberg method) determined statistical significance and $|\log_2(FC)| > 1.0$ was selected to identify differentially expressed genes (DEGs). Pathway analysis by statistical overrepresentation was performed with DEGs separately for upregulated and downregulated genes with the Gene Ontology (GO) database using the Rapid Integration of Term Annotation and Network (RITAN) package v1.26.0577 (https://bioconductor.org/packages/release/bioc/html/RITAN.html). A two-sided adjusted p-value (q-value) threshold of 0.05 (Benjamini-Hochberg method) was used to determine statistically overrepresented pathways.

Image analysis

Images were processed and analyzed with imageJ2 V2.14.0/1.54f. The "*Analyze Particles*" and "*Nucleus Counter*" plugins were used for aggregate size and number analysis; "*Analyze Skeleton*" was used for primary neuron neurite length quantification. The fluorescence intensity measurement was used to determine striatal TH projection intensity.

Quantification and statistical analysis

Data are presented as mean ± SEM and were derived from at least three independent experiments. Information on replicates (n) is given in figure legends. Statistical analysis was performed using the unpaired t-test, also known as Student's t-test (comparing two groups) or ANOVA with Dunnett test (comparing multiple groups against control). Distributions of raw data approximated normal distributions.

944 **References:**

945 1. Ross, C. A. & Poirier, M. A. Protein aggregation and neurodegenerative disease. *Nat Med*
946 **10**, S10–S17 (2004).
947 2. Soto, C. & Pritzkow, S. Protein misfolding, aggregation, and conformational strains in
948 neurodegenerative diseases. *Nat Neurosci* **21**, 1332–1340 (2018).
949 3. Goedert, M., Clavaguera, F. & Tolnay, M. The propagation of prion-like protein inclusions
950 in neurodegenerative diseases. *Trends in Neurosciences* **33**, 317–325 (2010).
951 4. Marsh, A. P. Molecular mechanisms of proteinopathies across neurodegenerative disease: a
952 review. *Neurological Research and Practice* **1**, 35 (2019).
953 5. Jucker, M. & Walker, L. C. Self-propagation of pathogenic protein aggregates in
954 neurodegenerative diseases. *Nature* **501**, 45–51 (2013).
955 6. Spillantini, M. G., Crowther, R. A., Jakes, R., Hasegawa, M. & Goedert, M. α-Synuclein in
956 filamentous inclusions of Lewy bodies from Parkinson's disease and dementia with Lewy
957 bodies. *Proceedings of the National Academy of Sciences* **95**, 6469–6473 (1998).
958 7. Del Rey, N. L.-G. *et al.* Advances in Parkinson's Disease: 200 Years Later. *Frontiers in*
959 *Neuroanatomy* **12**, (2018).
960 8. Postuma, R. B. & Berg, D. Advances in markers of prodromal Parkinson disease. *Nat Rev*
961 *Neurol* **12**, 622–634 (2016).
962 9. Calabresi, P. *et al.* Alpha-synuclein in Parkinson's disease and other synucleinopathies: from
963 overt neurodegeneration back to early synaptic dysfunction. *Cell Death Dis* **14**, 1–16 (2023).
964 10. Surmeier, D. J., Obeso, J. A. & Halliday, G. M. Selective neuronal vulnerability in Parkinson
965 disease. *Nat Rev Neurosci* **18**, 101–113 (2017).

966 11. Jackson-Lewis, V., Blesa, J. & Przedborski, S. Animal models of Parkinson's disease.
967 *Parkinsonism Relat Disord* **18 Suppl 1**, S183-185 (2012).
968 12. Konnova, E. A. & Swanberg, M. Animal Models of Parkinson's Disease. in *Parkinson's*
969 *Disease: Pathogenesis and Clinical Aspects* (eds. Stoker, T. B. & Greenland, J. C.) (Codon
970 Publications, Brisbane (AU), 2018).
971 13. Dovonou, A. *et al.* Animal models of Parkinson's disease: bridging the gap between disease
972 hallmarks and research questions. *Translational Neurodegeneration* **12**, 36 (2023).
973 14. Bové, J. & Perier, C. Neurotoxin-based models of Parkinson's disease. *Neuroscience* **211**,
974 51–76 (2012).
975 15. Bové, J., Prou, D., Perier, C. & Przedborski, S. Toxin-induced models of Parkinson's
976 disease. *Neurotherapeutics* **2**, 484–494 (2005).
977 16. Dawson, T. M., Ko, H. S. & Dawson, V. L. Genetic Animal Models of Parkinson's Disease.
978 *Neuron* **66**, 646–661 (2010).
979 17. Chung, H. K., Ho, H.-A., Pérez-Acuña, D. & Lee, S.-J. Modeling α-Synuclein Propagation
980 with Preformed Fibril Injections. *JMD* **12**, 139–151 (2019).
981 18. Chmielarz, P. & Domanskyi, A. Alpha-synuclein preformed fibrils: a tool to understand
982 Parkinson's disease and develop disease modifying therapy. *Neural Regeneration Research*
983 **16**, 2219 (2021).
984 19. Polinski, N. K. A Summary of Phenotypes Observed in the In Vivo Rodent Alpha-Synuclein
985 Preformed Fibril Model. *J Parkinsons Dis* **11**, 1555–1567.
986 20. Armstrong, R. A., Lantos, P. L. & Cairns, N. J. What determines the molecular composition
987 of abnormal protein aggregates in neurodegenerative disease? *Neuropathology* **28**, 351–365
988 (2008).

989 21. Mahul-Mellier, A.-L. *et al.* The process of Lewy body formation, rather than simply α-
990 synuclein fibrillization, is one of the major drivers of neurodegeneration. *Proceedings of the*
991 *National Academy of Sciences* **117**, 4971–4982 (2020).
992 22. Shen, H. *et al.* De novo design of self-assembling helical protein filaments. *Science* **362**,
993 705–709 (2018).
994 23. Fallas, J. A. *et al.* Computational design of self-assembling cyclic protein homo-oligomers.
995 *Nature Chem* **9**, 353–360 (2017).
996 24. Garcia-Seisdedos, H., Empereur-Mot, C., Elad, N. & Levy, E. D. Proteins evolve on the edge
997 of supramolecular self-assembly. *Nature* **548**, 244–247 (2017).
998 25. Chen, Y. X. *et al.* Structural Determination of a Filamentous Chaperone to Fabricate
999 Electronically Conductive Metalloprotein Nanowires. *ACS Nano* **14**, 6559–6569 (2020).
1000 26. Lin, D. *et al.* Time-tagged ticker tapes for intracellular recordings. *Nat Biotechnol* **41**, 631–
1001 639 (2023).
1002 27. Linghu, C. *et al.* Recording of cellular physiological histories along optically readable self-
1003 assembling protein chains. *Nat Biotechnol* **41**, 640–651 (2023).
1004 28. Chen, X. *et al.* Functional gene delivery to and across brain vasculature of systemic AAVs
1005 with endothelial-specific tropism in rodents and broad tropism in primates. *Nat Commun* **14**,
1006 3345 (2023).
1007 29. Shay, T. F. *et al. Human Cell Surface-AAV Interactomes Identify LRP6 as Blood-Brain-*
1008 *Barrier Transcytosis Receptor and Immune Cytokine IL3 as AAV9 Binder*.
1009 http://biorxiv.org/lookup/doi/10.1101/2024.01.05.574399 (2024)
1010 doi:10.1101/2024.01.05.574399.

1011 30. Yang, H. & Hu, H.-Y. Sequestration of cellular interacting partners by protein aggregates:
1012 implication in a loss-of-function pathology. *The FEBS Journal* **283**, 3705–3717 (2016).
1013 31. Hartmann, A. Postmortem studies in Parkinson's disease. *Dialogues in Clinical*
1014 *Neuroscience* **6**, 281 (2004).
1015 32. Wakabayashi, K. *et al.* The Lewy Body in Parkinson's Disease and Related
1016 Neurodegenerative Disorders. *Mol Neurobiol* **47**, 495–508 (2013).
1017 33. Moors, T. E. & Milovanovic, D. Defining a Lewy Body: Running Up the Hill of Shifting
1018 Definitions and Evolving Concepts. *Journal of Parkinson's Disease* **14**, 17 (2024).
1019 34. Urrestizala-Arenaza, N., Cerchio, S., Cavaliere, F. & Magliaro, C. Limitations of human
1020 brain organoids to study neurodegenerative diseases: a manual to survive. *Front Cell*
1021 *Neurosci* **18**, 1419526 (2024).
1022 35. Makin, S. Pathology: The prion principle. *Nature* **538**, S13–S16 (2016).
1023 36. Goedert, M. Alzheimer's and Parkinson's diseases: The prion concept in relation to
1024 assembled Aβ, tau, and α-synuclein. *Science* **349**, 1255555 (2015).
1025 37. Frieg, B. *et al.* Quaternary structure of patient-homogenate amplified α-synuclein fibrils
1026 modulates seeding of endogenous α-synuclein. *Commun Biol* **5**, 1–10 (2022).
1027 38. Fares, M. B., Jagannath, S. & Lashuel, H. A. Reverse engineering Lewy bodies: how far
1028 have we come and how far can we go? *Nat Rev Neurosci* **22**, 111–131 (2021).
1029 39. Kim, T. W. *et al.* TNF-NF-κB-p53 axis restricts *in vivo* survival of hPSC-derived dopamine
1030 neurons. *Cell* **187**, 3671-3689.e23 (2024).
1031 40. Fiorini, M. R., Dilliott, A. A., Thomas, R. A. & Farhan, S. M. K. Transcriptomics of Human
1032 Brain Tissue in Parkinson's Disease: a Comparison of Bulk and Single-cell RNA
1033 Sequencing. *Mol Neurobiol* (2024) doi:10.1007/s12035-024-04124-5.

1034 41. Wang, J. *et al.* Biallelic *FDXR* mutations induce ferroptosis in a rare mitochondrial disease
1035 with ataxia. *Free Radical Biology and Medicine* (2025)
1036 doi:10.1016/j.freeradbiomed.2025.02.012.
1037 42. Chan, K. Y. *et al.* Engineered AAVs for efficient noninvasive gene delivery to the central
1038 and peripheral nervous systems. *Nat Neurosci* **20**, 1172–1179 (2017).
1039 43. Surmeier, D. J. Determinants of dopaminergic neuron loss in Parkinson's disease. *FEBS J*
1040 **285**, 3657–3668 (2018).
1041 44. Yang, Y. *et al.* Structures of α-synuclein filaments from human brains with Lewy pathology.
1042 *Nature* **610**, 791–795 (2022).
1043 45. Azcorra, M. *et al.* Unique functional responses differentially map onto genetic subtypes of
1044 dopamine neurons. *Nat Neurosci* **26**, 1762–1774 (2023).
1045 46. Kamath, T. *et al.* Single-cell genomic profiling of human dopamine neurons identifies a
1046 population that selectively degenerates in Parkinson's disease. *Nat Neurosci* **25**, 588–595
1047 (2022).
1048 47. Andréll, J. *et al.* Crystal Structure of the Acid-Induced Arginine Decarboxylase from
1049 Escherichia coli: Reversible Decamer Assembly Controls Enzyme Activity. *Biochemistry* **48**,
1050 3915–3927 (2009).
1051 48. Challis, R. C. *et al.* Systemic AAV vectors for widespread and targeted gene delivery in
1052 rodents. *Nat Protoc* **14**, 379–414 (2019).
1053 49. Lock, M., Alvira, M. R., Chen, S.-J. & Wilson, J. M. Absolute determination of single-
1054 stranded and self-complementary adeno-associated viral vector genome titers by droplet
1055 digital PCR. *Hum Gene Ther Methods* **25**, 115–125 (2014).

1056 50. Fan, Y. *et al.* hPSC-derived sacral neural crest enables rescue in a severe model of
1057 Hirschsprung's disease. *Cell Stem Cell* **30**, 264-282.e9 (2023).
1058 51. Lancaster, M. A. & Knoblich, J. A. Generation of cerebral organoids from human pluripotent
1059 stem cells. *Nat Protoc* **9**, 2329–2340 (2014).
1060